

A GLIMPSE into the UV Continuum Slopes of the Faintest Galaxies in the Epoch of Reionization

MICHELLE C. JECMEN,^{1,2} JOHN CHISHOLM,^{1,2} HAKIM ATEK,³ VASILY KOKOREV,^{1,2} RYAN ENDSLEY,^{1,2}
 IRYNA CHEMERYNSKA,³ LUKAS J. FURTAK,^{1,2} RICHARD PAN,⁴ SEIJI FUJIMOTO,^{5,6} ROHAN P. NAIDU,^{7,*}
 JULIAN B. MUÑOZ,^{1,2} ANGELA ADAMO,⁸ YOSHIHISA ASADA,^{9,6} ARGHYADEEP BASU,¹⁰ DANIELLE A. BERG,^{11,2}
 JEREMY BLAIZOT,¹⁰ MIROSLAVA DESSAUGES-ZAVADSKY,¹² EMMA GIOVINAZZO,¹³ TIGER YU-YANG HSIAO,^{1,2}
 HARLEY KATZ,^{14,15} DAMIEN KORBER,¹³ JED MCKINNEY,^{1,2,*} KRISTEN. B. W. MCQUINN,^{16,17} PASCAL A. OESCH,^{12,18} AND
 DANIEL SCHÄFER¹²

¹Department of Astronomy, The University of Texas at Austin, Austin, TX 78712, USA

²Cosmic Frontier Center, The University of Texas at Austin, Austin, TX 78712, USA

³Institut d'Astrophysique de Paris, CNRS, Sorbonne Université, 98bis Boulevard Arago, 75014, Paris, France

⁴Department of Physics & Astronomy, Tufts University, MA 02155, USA

⁵David A. Dunlap Department of Astronomy and Astrophysics,

University of Toronto, 50 St. George Street, Toronto, Ontario, M5S 3H4, Canada

⁶Dunlap Institute for Astronomy and Astrophysics, 50 St. George Street, Toronto, Ontario, M5S 3H4, Canada

⁷MIT Kavli Institute for Astrophysics and Space Research, 70 Vassar Street, Cambridge, MA 02139, USA

⁸Department of Astronomy, The Oskar Klein Centre, Stockholm University, AlbaNova, SE-10691 Stockholm, Sweden

⁹David A. Dunlap Department of Astronomy and Astrophysics, University of Toronto, 50 St. George Street, Toronto, Ontario, M5S 3H4, Canada

¹⁰Univ Lyon, Univ Lyon1, Ens de Lyon, CNRS, CRAL UMR5574, F-69230, Saint-Genis-Laval, France

¹¹Department of Astronomy, The University of Texas at Austin, 2515 Speedway, Stop C1400, Austin, TX 78712, USA

¹²Department of Astronomy, University of Geneva, Chemin Pegasi 51, 1290 Versoix, Switzerland

¹³Observatoire de Genève, Université de Genève, Chemin Pegasi 51, 1290 Versoix, Switzerland

¹⁴Department of Astronomy & Astrophysics, University of Chicago, 5640 S Ellis Avenue, Chicago, IL 60637, USA

¹⁵Kavli Institute for Cosmological Physics, University of Chicago, Chicago IL 60637, USA

¹⁶Space Telescope Science Institute, 3700 San Martin Drive, Baltimore, MD, 21218, USA

¹⁷Rutgers University, Department of Physics and Astronomy, 136 Frelinghuysen Road, Piscataway, NJ 08854, USA

¹⁸Cosmic Dawn Center (DAWN), Niels Bohr Institute, University of Copenhagen, Jagtvej 128, København N, DK-2200, Denmark

(Received n/a; Revised n/a; Accepted n/a)

Submitted to ApJ

ABSTRACT

As observations have yet to constrain the ionizing properties of the faintest ($M_{\text{UV}} \gtrsim -16$) galaxies, their contribution to cosmic reionization remains unclear. The rest-frame ultraviolet (UV) continuum slope (β) is a powerful diagnostic of stellar populations and one of the few feasible indicators of the escape fraction of ionizing photons (f_{esc}) for such faint galaxies at high-redshift. Leveraging ultra-deep JWST/NIRCam GLIMPSE imaging of strong lensing field Abell S1063, we estimate UV continuum slopes of 555 galaxies at $z > 6$ with absolute magnitudes down to $M_{\text{UV}} \simeq -12.5$. We find a modest evolution of β with redshift and a flattening in the β - M_{UV} relation such that galaxies fainter than $M_{\text{UV}} \sim -16.5$ no longer exhibit the bluest UV slopes. The 138 ultra-faint galaxies with $M_{\text{UV}} > -16$ are a diverse population encompassing dusty (30%), old (15%), and low-mass (50%) galaxies. We apply the empirical β - f_{esc} relation from local Lyman continuum leakers, finding the mean f_{esc} peaks at $\sim 20\%$ at $M_{\text{UV}} = -16.5$ and declines towards fainter galaxies, while remaining consistent with $f_{\text{esc}} = 14\%$ within uncertainties, in agreement with recent radiative transfer simulations. Incorporating GLIMPSE constraints on the UV luminosity function, ionizing photon production efficiency, and escape fractions produces a reionization history consistent with independent observational constraints. Our

results indicate galaxies with M_{UV} between -18 and -14 supplied $\sim 60\%$ of the ionizing photons to cosmic reionization, while the lower f_{esc} of fainter galaxies produces a natural cutoff in the ionizing photon production rate density.

Keywords: galaxies: high-redshift — cosmology:reionization — galaxies: evolution — ISM: dust

1. INTRODUCTION

Cosmic reionization marks the final major phase transition of the universe, during which hydrogen in the intergalactic medium (IGM) transforms from largely neutral to ionized. Reionization progresses as Lyman continuum (LyC) photons emitted by the first luminous sources ionize the surrounding hydrogen, creating expanding ionized bubbles that eventually coalesce to form a predominantly ionized universe by $z \sim 6$ (Fan et al. 2006; Planck Collaboration et al. 2016; Robertson 2022). This process heats the IGM, regulates galaxy growth, and establishes the conditions for large-scale structure formation (Gnedin 2000; McQuinn 2016).

The timing and morphology of reionization depend sensitively on the abundance and spatial distribution of the sources which contributed the requisite ionizing photons (Ouchi et al. 2009a; Robertson et al. 2013; Madau & Haardt 2015; Robertson et al. 2015). A reionization scenario dominated by numerous, evenly distributed sources would produce a relatively spatially uniform ionization field, whereas one driven by fewer, more clustered sources would result in a patchier, more inhomogeneous progression (Finkelstein et al. 2019; Naidu et al. 2020). This distinction is crucial, as reionization morphology determines subsequent galaxy formation and growth and impacts the cosmic microwave background (CMB) and Lyman- α forest measurements (e.g., Mason et al. 2019).

The leading sources of reionization are thought to be star-forming galaxies (e.g., Ouchi et al. 2009b; Robertson et al. 2013, 2015; Bouwens et al. 2015a; Finkelstein et al. 2019; Naidu et al. 2020) with active galactic nuclei (AGN) contributing at later times ($z \simeq 5\text{-}7$; e.g., Madau & Haardt 2015; Grazian et al. 2024; Madau et al. 2024; Singha et al. 2025). However, each of these sources have their theoretical challenges. Star-forming galaxies are widespread and abundant but individually produce relatively few ionizing photons (e.g., Begley et al. 2022), many of which are absorbed by surrounding neutral gas and dust within the galaxy (Gnedin et al. 2008; Bouwens et al. 2015b). In contrast, AGN are efficient ionizing sources (Giallongo et al. 2015; Grazian et al. 2018) but

are less common than star-forming galaxies and previously thought to only form well into reionization.

Quantifying the contribution of star-forming galaxies to reionization requires constraining the ionizing emissivity (\dot{n}_{ion}), often expressed as

$$\dot{n}_{\text{ion}} = \int \phi_{\text{UV}} \xi_{\text{ion}} L_{\text{UV}} f_{\text{esc}} dM_{\text{UV}} \quad (1)$$

where ϕ_{UV} is the UV luminosity function (UVLF), ξ_{ion} is the intrinsic production rate of ionizing photons per UV continuum luminosity (L_{UV}), and f_{esc} is the fraction of LyC photons which escape into the IGM. Each of these factors is expected to vary with both redshift and galaxy properties (e.g. absolute magnitude, stellar mass, star-formation rate).

Faint, low-mass galaxies have long been compelling candidates for dominating \dot{n}_{ion} during the Epoch of Reionization (EoR). In hierarchical structure formation, such galaxies are abundant at early times, driving a steep increase in ϕ_{UV} toward faint magnitudes (Bouwens et al. 2014; Finkelstein et al. 2015; Atek et al. 2015). Their low metallicities and bursty star-formation histories yield high ξ_{ion} (e.g., Endsley et al. 2023), while their low dust content and shallow gravitational potentials enable stellar feedback to efficiently remove neutral hydrogen to promote higher f_{esc} than in massive systems (Treibitsch et al. 2017; Rosdahl et al. 2022). Taken together, these properties imply that large populations of faint galaxies at high redshift intrinsically produce substantial ionizing radiation and efficiently leak it into the IGM, thereby powering reionization. These faint galaxies have long been theorized as the dominant contributors to reionization, but have always been beyond observational constraints (Finkelstein et al. 2012a; Robertson et al. 2013).

Initial JWST observations suggest galaxies in the early universe were more prolific producers of ionizing photons than previously anticipated. The overabundance of bright galaxies at early times results in minimal evolution in the bright-end of the galaxy UV luminosity function (e.g. Naidu et al. 2022; Finkelstein et al. 2023; Harikane et al. 2023; Donnan et al. 2023). In addition, initial measurements of ξ_{ion} at $z > 5$ revealed a population of extremely efficient producers of ionizing photons (Endsley et al. 2023; Prieto-Lyon et al. 2023; Simmonds et al. 2023; Atek et al. 2024), however subsequent analysis has revealed a more complex picture where low-mass

* NASA Hubble Fellow

galaxies undergo extremely episodic “bursty” star formation histories (Pahl et al. 2023; Endsley et al. 2024; Simmonds et al. 2024). Collectively these findings, when extrapolated to include fainter galaxies, imply a much larger ionizing emissivity which produces a reionization history that evolves too rapidly compared to constraints from the CMB and Lyman- α forest (Muñoz et al. 2024).

To reconcile this tension, several explanations have been proposed: over-predicted average ξ_{ion} values from bursty low-mass galaxies (Simmonds et al. 2024; Pahl et al. 2023), overestimated f_{esc} in faint galaxies (Papovich et al. 2025), or a higher IGM clumping factor (Davies et al. 2024). However, the faintest galaxies (hereafter defined as $M_{\text{UV}} \gtrsim -16$) at $z > 6$ remain largely unobserved, leaving their true contribution to reionization uncertain.

A key challenge is constraining f_{esc} . Direct measurements of f_{esc} at $z \gtrsim 4$ are statistically unlikely due to absorption from neutral hydrogen in the IGM (Inoue et al. 2014). Instead, local analogs of LyC leakers have been studied in-depth, suggesting that galaxies with high f_{esc} exhibit minimal line-of-sight interstellar medium (ISM) absorption, high ionization emission-lines, and compact star-formation (Izotov et al. 2016b,a, 2018b,a; Steidel et al. 2018; Begley et al. 2022; Chisholm et al. 2022; Flury et al. 2022a,b; Mascia et al. 2023; Pahl et al. 2023; Jaskot et al. 2024a,b). Several diagnostics have been proposed based on these trends, including small Ly α peak separations (Verhamme et al. 2015), compact Ly α halos (Saldana-Lopez et al. 2025), Mg II emission (Henry et al. 2018; Chisholm et al. 2020; Gazagnes et al. 2025), high [O III]/[O II] ratio (Izotov et al. 2018b), and blue UV continuum slopes (Chisholm et al. 2022).

The UV continuum slope (β , where $F_{\lambda} \propto \lambda^{\beta}$) is a promising population-level probe of f_{esc} in faint, high-redshift galaxies. A galaxy’s intrinsic UV slope is set by the massive star population and limited to blue values between -3.0 and -2.5 for stellar populations younger than 50 Myr, varying according to metallicity and age (e.g. Schaefer & Pelló 2005; Katz et al. 2025a). The observed UV slope is reddened by the addition of nebular continuum to average values of $\beta \sim -2.6$, but can reach $\beta \sim -1.0$ in extreme nebular continuum systems (Katz et al. 2025a). Typically, the UV slope traces and is reddened most substantially by dust attenuation, producing values of $\beta \sim -2.0$ with even small $E(\text{B-V}) \sim 0.04$ mag. As such, red UV continuum slopes indicate the presence of dust, which is an efficient tracer of cool gas and strongly absorbs ionizing photons. Thus, redder UV slopes have been empirically shown at low-redshift to correlate with lower f_{esc} values (Chisholm et al. 2022).

In contrast, UV slopes bluer than $\beta \sim -2.8$ cannot be reddened by dust and gas, suggesting high f_{esc} .

The UV continuum slope has been widely studied for galaxies between $z \simeq 2 - 9$ with both HST (e.g. Dunlop et al. 2012; Finkelstein et al. 2012b; Rogers et al. 2013; Dunlop et al. 2013; Bouwens et al. 2014; Morales et al. 2023; Bhatawdekar & Conselice 2021) and JWST (Cullen et al. 2023; Nanayakkara et al. 2023; Morales et al. 2024; Topping et al. 2024; Austin et al. 2024; Saxena et al. 2024; Donnan et al. 2025). In general, the population average β becomes bluer at higher redshifts ($\langle \beta \rangle \sim -1.8$ at $z \sim 4$ to $\langle \beta \rangle \sim -2.4$ at $z \sim 7$; e.g. Finkelstein et al. 2012a), likely reflecting reduced dust content or grayer dust attenuation curves (McKinney et al. 2025). Many studies find β also decreases towards fainter galaxies and/or lower stellar masses (Bouwens et al. 2012; Bhatawdekar & Conselice 2021; Nanayakkara et al. 2023; Saldana-Lopez et al. 2023; Topping et al. 2024; Dottorini et al. 2025), although these measurements are biased by photometric scatter and have yet to probe galaxies fainter than $M_{\text{UV}} \sim -16$ (Cullen et al. 2023; Austin et al. 2024; Morales et al. 2024).

This work aims to use the UV continuum slopes to provide the first direct, population-level estimates of f_{esc} for galaxies fainter than $M_{\text{UV}} \sim -16$ in the EoR. While the most robust f_{esc} estimates require a multivariate approach, Jaskot et al. (2024b) shows that the UV slope and neutral gas tracers share the most predictive power for f_{esc} . The UV slope allows us to test the long-standing assumption that the faintest galaxies exhibit the highest escape fractions as a starting point to understanding their contribution to cosmic reionization.

Throughout this work we analyze data from the JWST GLIMPSE survey (Atek et al. 2025), a program which leverages ultra-deep imaging and strong gravitational lensing to estimate UV slopes from the faintest galaxies in the EoR. In Section 2, we describe the observations and sample selections. Section 3 outlines our methods for measuring β and we present our results for how β evolves with redshift and absolute magnitude in Section 4. We present the diversity of faint galaxies in our sample and evidence for extremely blue UV slopes, followed by a discussion of the estimated escape fractions and their implications on cosmic reionization in Section 5. We conclude with a summary of key findings in Section 6. Throughout this paper we assume a flat Λ CDM cosmology with $H_0 = 70 \text{ km s}^{-1}$, $\Omega_m = 0.3$, and $\Omega_{\Lambda} = 0.7$. All magnitudes are AB.

2. OBSERVATIONS AND REDUCTIONS

Here we briefly describe the observations, data reductions, and sample selection. A fully detailed breakdown of these steps is given in [Atek et al. \(2025\)](#).

This work uses imaging data from the Cycle 2 JWST GLIMPSE survey (GO-3293, PIs: H. Atek & J. Chisholm). The program leverages ultra-deep imaging and strong gravitational lensing of the massive foreground cluster Abell S1063 to probe the faintest, high-redshift galaxies with ~ 155 total hours across 7 broadbands (F090W, F115W, F150W, F200W, F277W, F356W, F444W) and 2 medium-band (F410M, F480M) filters. All broadband images reach 5σ depths in $0\farcs2$ apertures of ~ 30.8 mag, requiring up to 40 hours of integration time. Combined with gravitational lensing, we reach intrinsically faint magnitudes down to $M_{\text{UV}} \sim -12.5$ with magnification $\mu \sim 34$ at $z \sim 6.7$.

The data reduction follows the procedure of [Endsley et al. \(2024\)](#) using the *JWST* Science Calibration Pipeline and Calibration Reference Data System (CRDS) files from `JWST_1293.PMAP`. This procedure includes additional corrections for cosmic rays, 1/f noise, wisp removal, artifact correction, and stray light subtraction. We construct our own flat field images using all public NIRCam images as of January 12, 2025 to remove correlated noise as a result of sub-pixel dithering, recovering up to 0.5 mag in depth for the long-wavelength filters. Following the methods of [Shipley et al. \(2018\)](#); [Weaver et al. \(2024\)](#), bright cluster galaxies (bCGs) and intracluster light (ICL) are modeled and subtracted from the image.

All images are convolved to the Point Spread Functions (PSF) of the F480M data using PSFs empirically derived using stars within the GLIMPSE NIRCam field. Sources are detected in inverse-variance weighted stacks of both short-wavelength (SW) channels (F090W, F115W, F150W, and F200W) and long-wavelength (LW) channels (F277W, F356W, and F444W). Both detection images crucially explore the UV properties of distant galaxies as extremely blue high-redshift galaxies might only be detected in the SW stacks. We use SOURCE EXTRACTOR ([Bertin & Arnouts 1996](#)) to define the locations of sources and then merge the SW and LW catalogs into a single catalog. We measure flux densities with $0.2''$ circular apertures, appropriate for the faint high-redshift sources.

Sources are selected with two complementary techniques. The first focuses on a narrow redshift range between $z \sim 6.1 - 6.6$ where the $\text{H}\alpha$ line is redshifted into the F480M filter, the strong [O III] lines are in the F356W filter, and the F410M samples continuum regions. At $z = 6.1 - 6.6$, we do not have a JWST Lyman

Break filter (e.g. F070W) and the available *HST* data do not cover the entire GLIMPSE field. This means that SED fitting relies on strong rest-frame optical features. We first fit the entire GLIMPSE catalog with EAZY using the standard `blue_sfhz_13` models while also including tailored BEAGLE models to sample older stellar populations (see Chisholm et al. in preparation). For every $z = 6.1 - 6.6$ galaxy that EAZY selects we also fit with BEAGLE and require both codes to have a $> 95\%$ probability that the sources are between redshifts of 5-7. We then visually inspect all photometric candidates to remove strong artifacts, sources near edges of the detectors, or individual strongly lensed clumps within galaxies. After all of these cuts, we are left with 94 photometrically selected galaxies at $z = 6.1 - 6.6$, but only 70 of these sources are *not* also selected by the Lyman break selection (see below). In Chisholm et al. (in preparation) we compute the completeness of the photo- z selection, finding that we are highly complete down to $M_{\text{UV}} \sim -15$, and this completeness does not significantly depend on the UV continuum slope. We refer the reader to Chisholm et al. (in preparation) for more details on this sample selection.

The second selection technique uses a combination of the Lyman break technique and EAZY photometric fitting (e.g., [Atek et al. 2023](#)). We use a color-color selection criterion that is separately defined for four redshift bins ($6 < z < 9$; $9 < z < 11$; $11 < z < 15$; $z > 15$) and requires a Lyman Break of at least 0.8 mag. We then fit the photometry of all Lyman Break selected sources with EASY to confirm the redshift, and visually inspect each source. These sources are used to calculate the GLIMPSE UVLF at $z > 9$ ([Chemerynska et al. 2025](#)) and $z < 6$ (Atek et al. in prep.), and their associated completeness estimates apply to this subsample. We refer the reader to [Kokorev et al. \(2025\)](#), [Chemerynska et al. \(2025\)](#), and [Atek et al. \(2015\)](#) for additional selection criteria and detection thresholds. In total, we are left with a full sample of 555 sources across redshifts from 6-16.

We use a new strong lensing model of the lensing cluster AS1063, following the methodology outlined by [Furtak et al. \(2023\)](#) and using the updated version of the [Zitrin et al. \(2015\)](#) parametric code, sometimes referred to as `Zitrin-analytic`. This is a fully analytic method, such that the model is not limited to a grid resolution. The total mass distribution of AS1063 is modeled as two smooth dark matter (DM) halos (following e.g. [Bergamini et al. 2019](#); [Beauchesne et al. 2024](#)), which are parametrized as pseudo-isothermal elliptical mass distributions (PIEMDs; [Kassiola & Kovner 1993](#)), and 303 cluster galaxies which are parametrized as dual pseudo-

isothermal ellipsoids (dPIEs; Elíasdóttir et al. 2007). We use 75 multiple images of 28 sources to constrain the lens model, which achieves an average lens plane image reproduction error of $\Delta_{\text{RMS}} = 0.54''$. For more details on the lens model, its methods, constraints, and results, we refer the reader to Furtak et al. (in prep.). The final lens model produces magnification values at each object’s coordinates and redshift, which we use to correct the observed magnitudes, stellar masses, and star-formation rates.

3. UV SLOPES

For all 555 sources, we fit BAGPIPES (Carnall et al. 2018) spectral energy distribution (SED) models to all seven broadband and two medium band filters. We adopt a constant star formation history, allowing galaxy ages to vary between 10-100 Myr. In addition, we include a young burst component with an age range of 1-10 Myr to approximate a simple non-parametric star formation history, allowing for bursty star formation theorized at high redshift. For each star formation history, the observed stellar mass formed is limited to $\log(M_*) \in [4, 11]$, which we then de-magnify to account for gravitational lensing. We apply dust attenuation following the Calzetti dust law (Calzetti et al. 2000) with a log prior extinction coefficient (A_V) in the range [1e-5, 2]. We adopt uniform priors on metallicity and ionization parameter within the ranges $Z/Z_\odot \in [0.001, 2.5]$ and $\log(U) \in [-3, -1]$, respectively. Reported photometric redshifts are adopted from the maximum-likelihood BAGPIPES model and uncertainties from the inner 68th percentile of the posterior distribution. Figure 1 shows the maximum-likelihood SEDs for representative galaxies which span the range of UV continuum slopes in our sample.

We measure the UV slope (β_{PL}) by fitting a power law ($f_\lambda \propto \lambda^\beta$; Calzetti et al. 1994) to the rest-frame UV photometry, similar to Dunlop et al. (2013); Rogers et al. (2014); Topping et al. (2024). We highlight the filters used and the resulting best-fit line from this fitting procedure in red for each source in Figure 1. We fit β_{PL} using all photometric filters with rest-frame pivot wavelengths in the range 1350Å - 3400Å, a window chosen to avoid Ly α and contamination from rest-frame optical nebular emission lines and stellar continuum features while maximizing filter coverage across redshift. The filters that cover the defined window shift systematically with redshift, as reported in Table 1. Roughly 90% of our sources are fit using three filters.

Uncertainties on β_{PL} are estimated via Monte Carlo resampling. For each galaxy, we perturb both the redshift and photometry within errors and refit β over 1000

Table 1. Filters used in calculating the UV slope for each galaxy redshift.

Redshift	Filters used to fit β_{PL}
$5.7 \leq z < 7.1$	F115W, F150W, F200W
$7.1 \leq z < 7.6$	F115W, F150W, F200W, F277W
$7.6 \leq z < 9.5$	F150W, F200W, F277W
$9.5 \leq z < 10.1$	F150W, F200W, F277W, F356W
$10.1 \leq z < 11.1$	F200W, F277W, F356W
$11.1 \leq z < 12$	F200W, F277W, F356W, F410M
$12 \leq z < 13.2$	F200W, F277W, F356W, F410M, F444W
$13.2 \leq z$	F277W, F356W, F410M, F444W, F480M

realizations. The 16th and 84th percentiles of the resulting β distribution define the lower and upper uncertainties, respectively. As discussed in Austin et al. (2024), calculating the UV slope directly from broadband photometry can be biased by the inclusion of UV line emission and photometric “up-scattering” of filters red-ward of the Lyman break into the detection threshold (see Section 4.2 for a discussion of how this bias affects our sample). As such, we validate our β measurement by additionally estimating β_{SED} by fitting a power-law to the rest-frame UV continuum of the maximum-likelihood BAGPIPES SED. As advocated by Finkelstein et al. (2012b), this method utilizes all nine filters and thus encodes optical nebular and stellar emission, as shown by the gray best-fit SED curves in Figure 1. These features constrain the massive star population capable of producing ionizing photons and can mitigate photometric scatter biasing β_{PL} toward unphysical blue values. For this measurement, we adopt the narrower rest-frame wavelength window of 1350Å-1800Å to more closely align with Chisholm et al. (2022) and apply a 2σ clipping of spectral pixels in the best-fit SED model to remove UV emission lines. We calculate β_{SED} across all 500 posterior samples from BAGPIPES, reporting the 16th and 84th percentiles of distribution as the uncertainties.

Figure 2 compares the distribution of UV slopes as measured from power-law fitting to photometry (β_{PL} , red) versus from the model SEDs (β_{SED} , blue). Most notably, β_{PL} has a much wider distribution which peaks at slightly bluer UV slopes ($\langle \beta_{\text{PL}} \rangle \sim -2.27$ compared to $\langle \beta_{\text{SED}} \rangle \sim -2.06$). As expected, we find both methods yield consistent values within 1σ for 64% of sources in the sample, primarily for $\beta > -2.5$ as illustrated by the alignment of the blue contour curves with the one-to-one ($\beta_{\text{PL}} = \beta_{\text{SED}}$) line in Figure 2. We find that SED fitting does not reproduce the very blue values of $\beta_{\text{PL}} < -2.75$ measured directly from photometry for even the

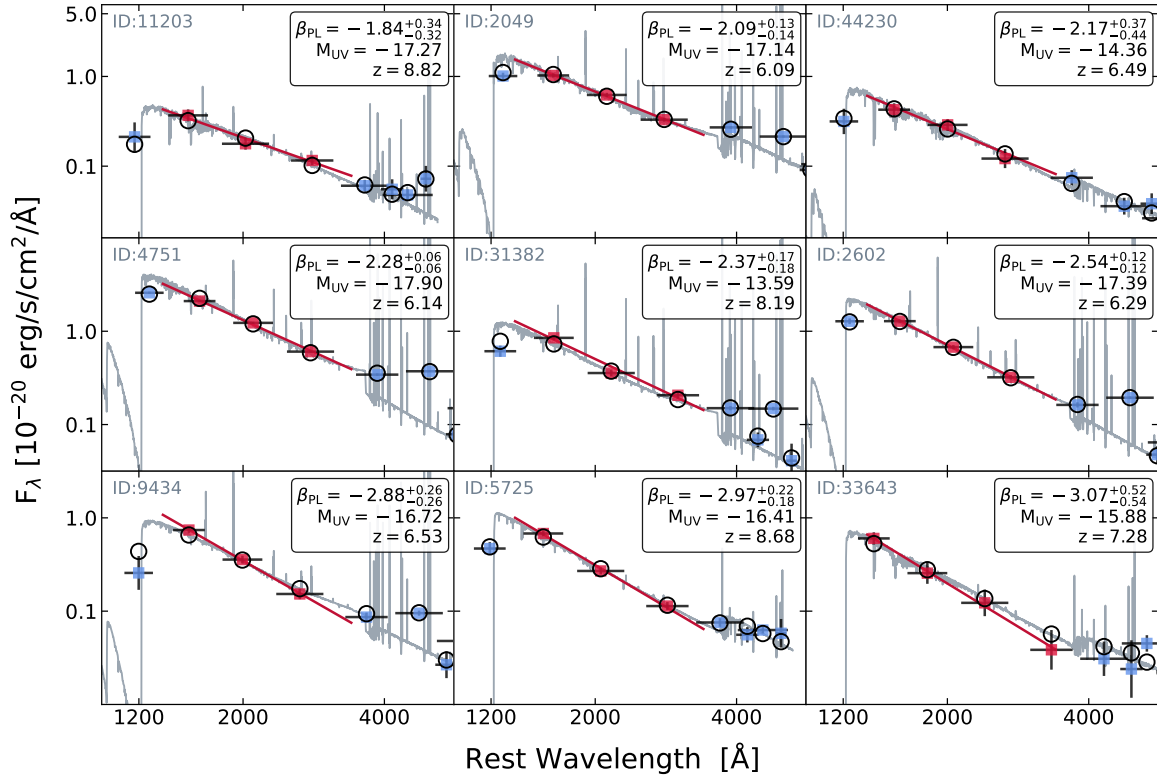


Figure 1. Representative galaxies ranging in UV slope (β_{PL}), absolute magnitude (M_{UV}), and photometric redshift (z) to illustrate the calculation of β_{PL} , ordered from reddest to bluest. Square points are observed photometry, colored red if used in power-law fitting (red line) and blue otherwise. The model SEDs are each shown in their rest-frame as gray curves with the predicted photometry as empty black circles. Most models can reproduce both the UV continuum and optical emission features, except for sources with extremely blue β_{PL} (bottom row).

youngest, metal-poor, and dust-free stellar populations (bottom row of Figure 1). This observed lower limit on β_{SED} is responsible for the deviation of the blue contours away from the one-to-one line.

We test if this lower limit on β_{SED} arises from the BAGPIPES requirement of zero ionizing photon escape, as explored in Morales et al. (2024); Austin et al. (2024); Giovinazzo et al. (2025). Even in dust-free models, ionizing photons must produce nebular continuum emission that reddens the UV slope, imposing a β_{SED} floor. To explore whether allowing for a non-zero escape fraction can reproduce our observed very blue β_{PL} , we additionally fit the adapted BAGPIPES model of Giovinazzo et al. (2025) which implements a simple “picket-fence” model of LyC escape. From these SEDs, we calculate β_{fesc} using the same procedure as β_{SED} , adopting a uniform prior on f_{esc} as to reproduce $\beta_{fesc} < -2.75$.

Adding f_{esc} as a free parameter results in a systematically bluer ($\langle \beta_{fesc} \rangle \sim -2.20$) distribution compared to

β_{SED} , as shown by the gray histogram and contours in Figure 2. We find that β_{fesc} and β_{PL} agree within 1σ for 78% of sources and that the adapted model can reproduce a UV continuum as blue as $\beta_{fesc} = -3.0$. However, we see that β_{fesc} is bluer than β_{PL} for galaxies with relatively red UV slopes, causing a worse agreement of the gray contour with the one-to-one line for red slopes in Figure 2. We further explore the impact of non-zero LyC escape on UV slopes in Section 5.2, where we examine our subset of galaxies with extremely blue UV slopes.

The UV slopes estimated from both SED models typically agree with our β_{PL} measurements within 1σ uncertainties, although neither method reproduces the full distribution inferred from photometry. We adopt β_{PL} as our fiducial UV slope estimation with the understanding that it may be impacted by photometric noise to include nonphysical values which cannot be explained by current SED modeling (see Section 4.2 for brief discussion of observational biases). This approach does not restrict the

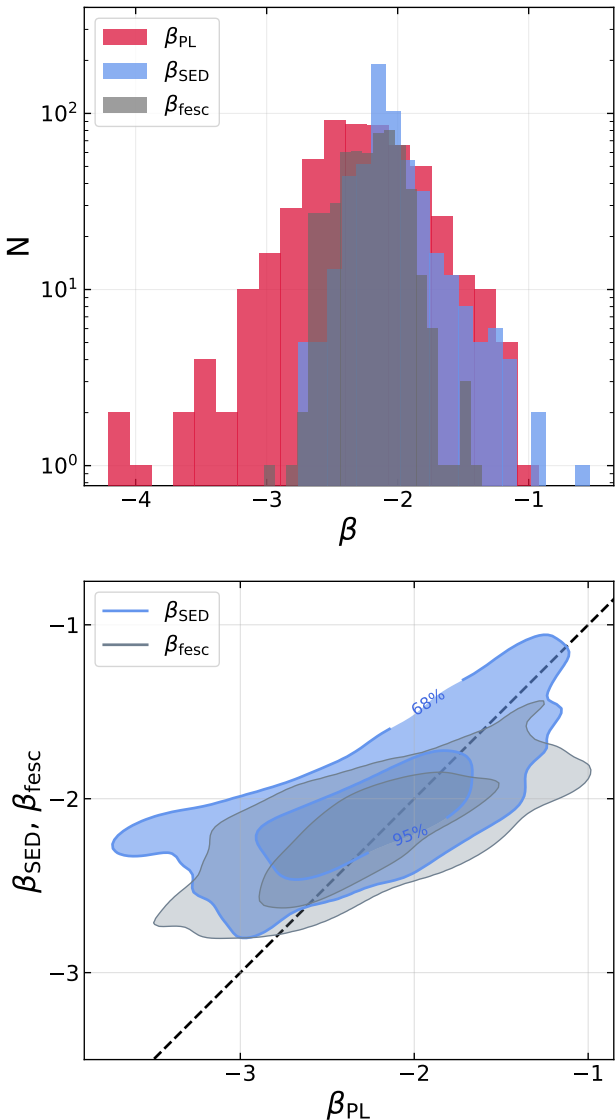


Figure 2. Comparison of UV slope measurements from power-law fits to photometry (β_{PL}) and to model SEDs with $f_{esc}=0$ (β_{SED}) and with varying f_{esc} (β_{fesc}). **Upper panel:** Histograms for each β_{PL} (red), β_{SED} (blue), and β_{fesc} (gray), with β_{PL} showing the widest distribution. **Lower panel:** Comparing the agreement of β_{PL} to the UV slope inferred from model SEDs for both β_{SED} (blue contours) and β_{fesc} (gray contours). Outer and inner contours enclose the 68th and 95th percentiles. The dashed black line indicates the one-to-one relation, from which contours deviate at very blue UV slopes not reproduced by models.

range of allowable UV slopes while allowing uncertainties to reflect the photometric noise. Throughout we use the SED fits to test our conclusions, but overall they are largely insensitive to this choice of methodology. A subset of this sample and its derived properties are given in Table 5; the full table is available online.

4. RESULTS

4.1. Redshift Evolution of UV Slopes

In Figure 3 we show the evolution of β with photometric redshift for our full sample. To understand how the UV slope of a typical galaxy changes with redshift, we calculate the median redshift and UV slope of the 459 sources with robust β measurements (signal-to-noise ratio, S/N, ≥ 5) in three redshift intervals ($z = 6-8$, $8-10$, $10-12$). Bin uncertainties are estimated via bootstrap resampling: for each of 1000 iterations we resample with replacement, perturb redshifts and UV slopes within their uncertainties, re-bin the mock sample, and compute the standard deviation of each bin. The final bin errors are taken as the median of these standard deviations across all iterations. These median bins are plotted as red diamonds in Figure 3 and summarized in Table 2.

The median UV slopes become slightly bluer with increasing redshift, but remain consistent at the $1-\sigma$ level. This consistency remains when repeating the binning procedure with the full sample or with a stricter $S/N \geq 10$ cut. A Kendall's τ test yields $\tau = -0.056$ ($p = 0.05$), indicating no statistically significant decrease with redshift within our sample. However, we highlight the lack of red galaxies at high redshift: only $11 \pm 5.1\%$ of galaxies at $z \geq 9$ have $\beta > -2.0$, compared to $27 \pm 2.3\%$ as $z \leq 7$.

We further fit a linear redshift relation to all individual sources, finding $d\beta/dz = -0.047 \pm 0.014$. This is consistent with Topping et al. (2024) ($d\beta/dz = -0.030^{+0.024}_{-0.029}$) and Roberts-Borsani et al. (2024) ($d\beta/dz = -0.06 \pm 0.01$), but much shallower than Cullen et al. (2024) ($d\beta/dz = -0.28^{+0.05}_{-0.05}$) at $z > 8$.

Finally, to explore whether the evolution of β is dependent on galaxy luminosity, as suggested in Topping et al. (2024), we split the sample into three M_{UV} bins: $M_{UV} < -17$, $-17 \leq M_{UV} \leq -15$, and $M_{UV} > -15$. At fixed M_{UV} , we find no significant difference in the redshift dependence of β in these M_{UV} sub-samples relative to the full sample.

Table 2. Median redshift, UV slope, M_{UV} and number of robust sources in each of the three redshift bins shown in Figure 3.

Redshift bin	z_{phot}	β	M_{UV}	N
$6 \leq z < 8$	6.67 ± 0.23	-2.28 ± 0.22	-16.8	379
$8 \leq z < 10$	8.54 ± 0.23	-2.46 ± 0.24	-16.4	63
$10 \leq z < 12$	11.1 ± 0.28	-2.52 ± 0.24	-16.7	14

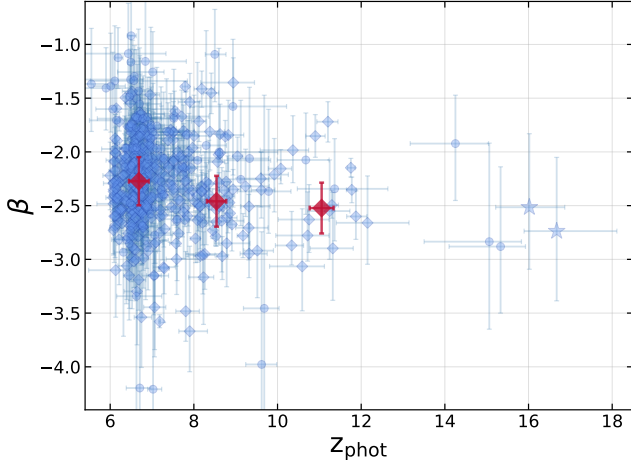


Figure 3. Mild evolution of β with redshift driven by a lack of red galaxies at high redshift. Red diamonds are median bins for galaxies with robust ($S/N \geq 5$) β measurements, plotted as blue diamonds. The two highest redshift sources (blue stars) are the high- z galaxy candidates of Kokorev et al. (2025).

4.2. $\beta - M_{UV}$ Relation

Due to the intrinsic depth reached by GLIMPSE, we measure the UV slopes of 138 galaxies with $M_{UV} \geq -16$, 88 of which have $S/N \geq 5$. In Figure 4, we show the dependence of β on M_{UV} for our full sample (blue points). To directly compare to brighter galaxies, we also calculate the UV slopes of the JADES photometric sample of Endsley et al. (2024) (gray points) following the methods outlined in Sections 3. The UV slopes of this JADES sample are independently calculated and fully analyzed in Topping et al. (2024); we include them here for comparison. Following the procedure described in Section 4.1, we bin all robust GLIMPSE+JADES UV slopes into equal-width M_{UV} intervals, with median values reported in Table 3. We note the large variance in UV slopes across all magnitudes, particularly near the detection threshold for unlensed galaxies ($M_{UV} \simeq -17$).

Consistent with previous studies (e.g. Cullen et al. 2023; Topping et al. 2024; Austin et al. 2024), we find that UV slopes initially become bluer towards fainter magnitudes over the range $M_{UV} \in [-22, -17]$. In this range, our median bins agree with the best-fit trends of Cullen et al. (2023); Topping et al. (2024) while remaining consistent with one another within their uncertainties. Furthermore, Zhao & Furlanetto (2024) fit a relation for the average UV slope as a function of both redshift and magnitude from the $z=4\text{-}8$ *HST* sample of Bouwens et al. (2014) and the $z=6\text{-}12$ JWST sample of Topping et al. (2024), both of which reach down to $M_{UV} \simeq -17$. We over-plot this decreasing relation for three

redshifts as the yellow curves in Figure 4, extrapolating to fainter magnitudes and capping β at -3.0 .

Notably, the decreasing trend of β with magnitude does not extend to fainter galaxies now observable with GLIMPSE. We find that *the faintest galaxies show UV slopes no bluer than those of brighter galaxies*. Indeed, our faintest bin at $M_{UV} = -14.4$ is consistent with all brighter median bins and lies $\sim 2\sigma$ above the extrapolated trend ($\langle \beta \rangle = -2.31$ compared to predicted $\beta \simeq -2.9$). Repeating the binning procedure including lower signal points drives the faintest bin even redder ($\langle \beta \rangle = -2.08$).

To test whether the $\beta - M_{UV}$ is better described by a simple trend or two distinct regimes, we fit both a single power-law and a smooth double power-law (SDPL) to the robust $S/N \geq 5$ GLIMPSE+JADES sample. We find the data is best represented by the smooth double-power law (red curve, Figure 4) given by:

$$\beta(M) = \frac{\beta_0}{[10^{-0.4(M-M^*)\alpha_1*n} + 10^{-0.4(M-M^*)\alpha_2*n}]^{1/n}}, \quad (2)$$

where $\beta_0 = -2.45 \pm 0.14$ is the normalization, $M^* = -18.5 \pm 1.00$ is the characteristic magnitude separating the bright- and faint-end behavior, $n = 11.5 \pm 16.6$ sets the sharpness of this transition, and $\alpha_1 = 0.11 \pm 0.06$ and $\alpha_2 = -0.01 \pm 0.02$ are the bright- and faint-end slopes, respectively. These values indicate that while bright galaxies get progressively bluer as luminosity decreases, galaxies fainter than $M_{UV} \sim -18$ either stay as blue as their brighter counterparts or get slightly redder. The SDPL fits the $S/N \geq 5$ data slightly better compared to a single power-law ($\chi^2_{\text{red,SDPL}} \sim 8.83$, $\chi^2_{\text{red,PL}} \sim 10.5$) with a $\Delta\text{BIC} = 21$ strongly favoring the SDPL fit. Hence, the faintest galaxies have UV slopes possibly redder, but at least no bluer than those of brighter galaxies.

Furthermore, this faint galaxy population is expected to have an average UV slope biased toward bluer values. First introduced by Dunlop et al. (2012), this ‘ β bias’ results when the filter red-ward of the Lyman break has its flux boosted into the detection threshold by photometric noise or scatter, resulting in an artificially bluer UV slope. This bias is most prominent for galaxies near the detection limit in a Lyman break selected sample where the filters used in source selection are also used in calculating β (Bouwens et al. 2012; Austin et al. 2024; Asada et al. 2025). Galaxies scattered to bluer values will be preferentially included, biasing the median UV slope to bluer values. Therefore, it is likely that the median UV slope of our faintest galaxies are even red-

der than observed, further reinforcing that the faintest galaxies do not have the bluest UV slopes.

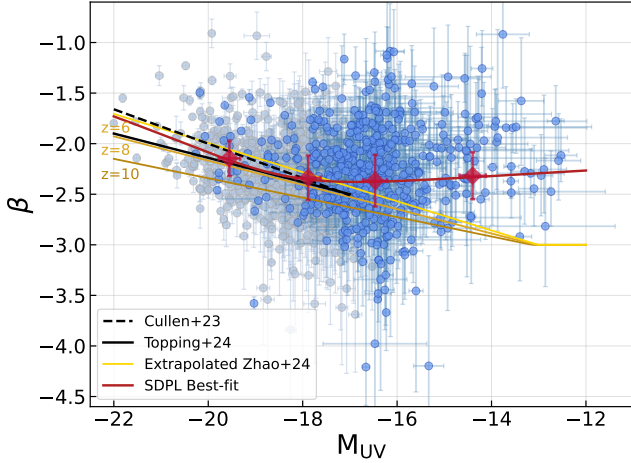


Figure 4. UV continuum slope versus M_{UV} , showcasing the redder UV slopes of the faintest galaxies. We plot the full GLIMPSE sample (blue circles) as well as the JADES photometric sample of Endsley et al. (2024) (gray circles). Red diamonds are median bins for robust UV slopes with $S/N \geq 5$ and the red curve is the best-fit of all robust points. Best-fit relations from Cullen et al. (2023); Topping et al. (2024) are plotted as solid and dashed black lines, respectively. Yellow lines show the combined *HST* + JWST sample of Zhao & Furlanetto (2024), extrapolated to fainter magnitudes for redshifts $z=6,8,10$.

Table 3. Median M_{UV} , UV slope, redshift, and number of robust GLIMPSE+JADES sources in each M_{UV} bin shown in Figure 4.

M_{UV} bin	M_{UV}	β	z_{phot}	N
$[-21, -19]$	-19.6 ± 0.23	-2.14 ± 0.17	6.68	224
$[-19, -17]$	-17.9 ± 0.27	-2.34 ± 0.22	6.87	654
$[-17, -15]$	-16.5 ± 0.25	-2.37 ± 0.25	6.77	264
$[-15, -13]$	-14.4 ± 0.28	-2.31 ± 0.23	7.17	28

5. DISCUSSION

We have presented the UV continuum slopes of GLIMPSE galaxies, highlighting the surprisingly redder β values of the faintest galaxies. Here we look more in-depth at both the variety of faint galaxies and galaxies with $\beta \leq -2.8$, contextualizing their UV slopes through their observed emission-line properties. We then justify and comment on the implied LyC escape fractions from these UV slopes, validating our findings by comparing to MEGATRON simulations of faint galaxies (Katz et al. 2025b). Finally, we discuss what the GLIMPSE obser-

vations of faint galaxies imply for the timing and drivers of cosmic reionization.

5.1. A Diverse Population of Faint Galaxies

The faintest galaxies are expected to have minimal dust, young ages, and low metallicity. These properties imply faint galaxies should have bluer UV slopes than brighter galaxies, as observed in the range $-20 < M_{\text{UV}} < -17$ for $z > 6$ with JWST (e.g. Cullen et al. 2023; Topping et al. 2024) and $z < 8$ with HST (Rogers et al. 2013; Bouwens et al. 2014). However, these properties have yet to be observationally verified for populations of galaxies with $M_{\text{UV}} \gtrsim -16$. By leveraging strong gravitational lensing and ultra-deep imaging with JWST, the GLIMPSE survey provides the first statistical view of the faintest galaxies in the early universe.

We detect 138 galaxies with $M_{\text{UV}} > -16$ and find a diverse population of faint galaxies. The UV slopes of faint galaxies span a wide range, with a dispersion of $\sigma_{\beta} = 0.45$ for median $\beta = -2.27$ and $M_{\text{UV}} = -15.1$. We also observe a broad range of rest-optical emission line strengths, as clearly emphasized in Figure 5 by the SEDs where the 410M or 480M filters cover [O III]+H β and H α emission. Furthermore, the maximum-likelihood BAGPIPES models for the faint sub-sample predict an extreme range of dust attenuation ($A_{\text{V}} \in [0, 1.05]$) and intrinsic total stellar mass ($\log(M_{\star}) \in [4.4, 8.1]$). The large variance in observed properties suggests that galaxies appear faint for multiple reasons: dust attenuation, old stellar populations, and/or low stellar masses.

The SEDs in Figure 5 highlight the most extreme examples of galaxies whose faint magnitudes are primarily driven by each of these three mechanisms. The left column shows faint galaxies with red UV slopes ($\beta \sim -1.3$) and strong rest-optical emission, representative of dusty galaxies undergoing strong star-formation. The middle column features faint galaxies with moderately blue UV slopes ($\beta \sim -2.2$), minimal line-emission, and prominent Balmer breaks, indicative of older stellar populations (> 10 Myr) with recently quenched star formation. BAGPIPES models predict their stellar populations were primarily formed in the older, constant star-formation component rather than the younger burst component, resulting in low burst-to-constant mass fractions ($M_{\text{b}}/M_{\text{c}}$). Lastly, and most commonly expected, the right column shows faint galaxies with blue UV slopes ($\beta \sim -2.5$) and strong line-emission, requiring low stellar masses to explain their faint magnitudes, as predicted by BAGPIPES.

Of course, most of our faint galaxies ($M_{\text{UV}} > -16$) are influenced by more than one of these factors (e.g. both old and low-mass), but we can broadly separate

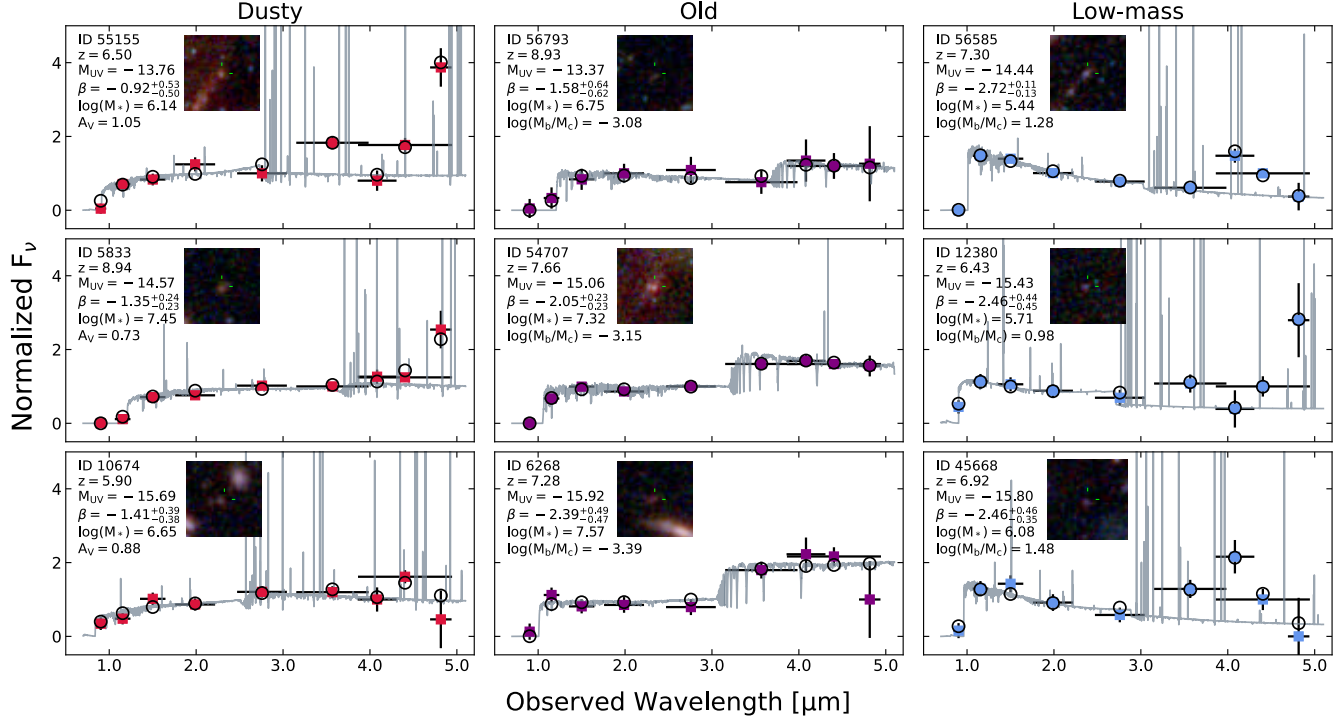


Figure 5. Notable faint ($M_{\text{UV}} > -16$) galaxies observed with GLIMPSE, selected to emphasize the diversity of this subsample. Each column showcases galaxies whose faint magnitudes are primarily driven by dust attenuation (left), older stellar populations (middle), and low stellar masses (right). For each galaxy, we compare the observed photometry (squares) to BAGPIPES model photometry (black circles) and show the best-fit SED as gray curves. We list A_V and intrinsic total stellar mass from the maximum-likelihood model. We also report the logarithmic ratio of the stellar mass formed in the recent burst to that formed in the older, constant star-formation component (M_b/M_c), indicating the relative mass-fraction of the stellar population.

our faint galaxy sample into these three populations. Around 30% of our faint sub-sample have UV slopes redder than -2.0 ($A_V \gtrsim 0.1$), suggesting measurable dust can be present in even the faintest systems at $z > 6$. Around 15% have predicted burst-to-constant mass fractions $M_b/M_c < 0.1$ from BAGPIPES, indicating the bulk of their stellar mass formed in older star formation episodes rather than recent bursts. The majority of our observed faint galaxies are low mass, with $\sim 50\%$ of the sub-sample having $\log(M_*/M_\odot) < 6$.

Although we see this diversity in galaxy properties, the scatter in UV slopes goes towards redder rather than bluer values. Only 26% of galaxies with $M_{\text{UV}} > -16$ have UV slopes bluer than -2.5 , and no galaxy fainter than $M_{\text{UV}} = -15$ has $\beta \leq -3.0$. Thus, we observe comparable numbers of dust-free and dusty faint galaxies. In comparison, slightly brighter galaxies with $M_{\text{UV}} \in [-19, -17]$ show a much lower fraction of red UV slopes (16% with $\beta > -2.0$) and a slightly higher fraction of blue slopes (30% with $\beta < -2.5$).

Overall, we find that faint galaxies are not a monolithic population, but rather encompass a range of stellar masses, dust content, and star-formation histories.

These GLIMPSE observations suggest that early dust production and bursty star formation histories complicate the interpretation of faint galaxies. We find that a single UV luminosity can translate to a diversity of galaxy properties, making it difficult to directly map the UVLF onto the halo mass function. The observed diversity in the faint-end UVLF agrees with past work that suggests stochastic star formation drives the over-abundance of UV-bright galaxies observed by JWST in the early universe (Mason et al. 2023; Kravtsov & Belokurov 2024; Gelli et al. 2024). Low-mass galaxies undergoing a strong burst of star-formation appear brighter than galaxies of similar mass undergoing more modest star formation. This scatters galaxies at fixed halo mass into different observed luminosities. The GLIMPSE observations suggest a similar scattering occurs due to dust, where galaxies in the early universe have a range of dust attenuation at fixed halo mass. Dustier galaxies will appear fainter than dust-free galaxies at the same halo mass. Therefore, both star formation history and dust production shift early galaxies to fainter or brighter magnitudes than theoretically predicted based on their halo masses.

5.2. Extremely Blue Objects

Galaxies with extremely blue UV continuum slopes ($\beta \leq -2.8$) are of particular interest, as standard population synthesis models with ionization-bounded conditions struggle to reproduce these very blue UV slopes (Raiter et al. 2010). Since β is reddened by nebular continuum and dust attenuation, an observed UV continuum bluer than $\beta \sim -2.8$ cannot be dominated by nebular continuum and must have no dust. Extremely blue UV slopes have been suggested to be caused by high LyC escape fractions or exotic stellar populations, but often result from photometric uncertainties (see Section 4.2).

We find 52 galaxies with $\beta \leq -2.8$ and assess whether their extremely blue UV slopes are robust. Figure 6 shows the six most robust extremely blue candidates, all of which have robust β measurements with $S/N > 5$ and observed photometry consistent within $1-\sigma$ with all model fluxes predicted by the adapted BAGPIPES model of Giovinazzo et al. (2025). For the majority of galaxies with $\beta \leq -2.8$, the UV slope uncertainties are large, with a median $\sigma_\beta = 0.49$, much larger than that of the full sample ($\sigma_\beta = 0.29$). From a visual inspection of each source, we find most extremely blue galaxies exhibit noisy SEDs, often with an unusually flat color between the F200W and F277W filters, suggesting F200W is under-measuring the flux and responsible for driving the UV slope artificially bluer, as shown in the upper left panel of Figure 6. Overall, we find that the majority of galaxies with extremely blue β values lack convincing evidence for such extreme slopes and can be explained by photometric uncertainty.

Furthermore, many of these galaxies have observed magnitudes near the $5-\sigma$ broadband detection threshold ($\langle M_{\text{obs}} \rangle = 30.07$ mag, $M_{\text{obs, thresh}} = 30.8$ mag), where extreme UV slopes can bias source selection (as discussed in Section 4.2). As most of these galaxies are also weakly magnified by gravitational lensing, this bias accounts for the increased variance in observed UV slopes at the corresponding absolute magnitude of $M_{\text{UV}} \simeq -17$ in Figure 4. Even with the increased depth of GLIMPSE, we do not find more convincing extreme UV slope candidates than shallower surveys (e.g. Cullen et al. 2024; Topping et al. 2024).

Notably, our extremely blue UV slopes are not from the faintest galaxies: only 13 (25%) sources with $\beta \leq -2.8$ have $M_{\text{UV}} > -16$. If these blue UV slopes were indicative of Population III objects or extreme low metallicity, we would expect to find them at the faintest magnitudes.

Although the majority of galaxies with extremely blue UV slopes have large uncertainties, we do identify indi-

vidual galaxies with compelling evidence for very blue β values driven by high LyC escape fractions. In the high f_{esc} scenario, there cannot be dust and ionizing photons are not absorbed by the hydrogen in the galaxy to create the nebular continuum, both of which strongly redden β . If our extremely blue UV slopes are indeed caused by high f_{esc} , they should have reduced rest-optical line-emission as shown by galaxies in the bottom row of Figure 6.

To further explore whether any extremely blue UV slopes in our sample indicate high LyC escape fractions, we analyze the BAGPIPES picket-fence model fits of Giovinazzo et al. (2025). Introducing f_{esc} as a free parameter allows the BAGPIPES model to reproduce an SED with both $\beta \leq -2.8$ and weak emission lines. As highlighted in the lower panel of Figure 2, we find that the varying f_{esc} model frequently results in an SED with a bluer slope, finding an average decrease of $\Delta\beta = -0.25$ for galaxies with extremely blue UV slopes. We compare the maximum likelihood SEDs for the zero f_{esc} model (gray curve) to the varying f_{esc} model (blue curve) for each galaxy in Figure 6. Allowing f_{esc} to vary only slightly improves the model fits, decreasing the median χ^2_ν from 0.67 to 0.64. This limited improvement while driving the UV slopes bluer is likely due to the age- f_{esc} degeneracy: galaxies with extremely blue UV slopes and weak emission lines could be explained as either high f_{esc} or a recently quenched B-Star dominated stellar population (Giovinazzo et al. 2025). With only photometry, it is difficult to disentangle these options.

Lastly, we have many galaxies with very blue, but not extreme, UV slopes of $\beta \sim -2.6$ that could have non-negligible LyC escape fractions. The JWST Director’s Discretionary Time program GLIMPSE-D (PID 9233; PIs: S. Fujimoto & R.P. Naidu) obtained deep (~ 30.4 hr) NIRSpec/MSA G395M observation of the Abell S1063 field, as detailed in S. Fujimoto et al. (in preparation). The spectra cover rest-frame H α for ~ 60 galaxies in our sample, most of which have no continuum emission detected. We highlight two galaxies observed by this program in Figure 7, showing both the GLIMPSE photometry and best-fit SEDs (upper panels) and zooming in on their NIRSpec H α emission. Both galaxies have similarly blue UV slopes ($\beta \sim -2.65$) but different rest-optical line-emission strengths. In the left panel, ID 21550 has no detected H α emission, with a rest-frame upper limit of $\text{EW}(\text{H}\alpha) \leq 137$ Å, confirming either a very high escape fraction or a ~ 10 Myr stellar population. In comparison, ID 6358 has moderately strong H α emission ($\text{EW}(\text{H}\alpha) = 860$ Å), as shown in the right panel, requiring recent star-formation while non-negligible LyC escape remains feasible. These spectro-

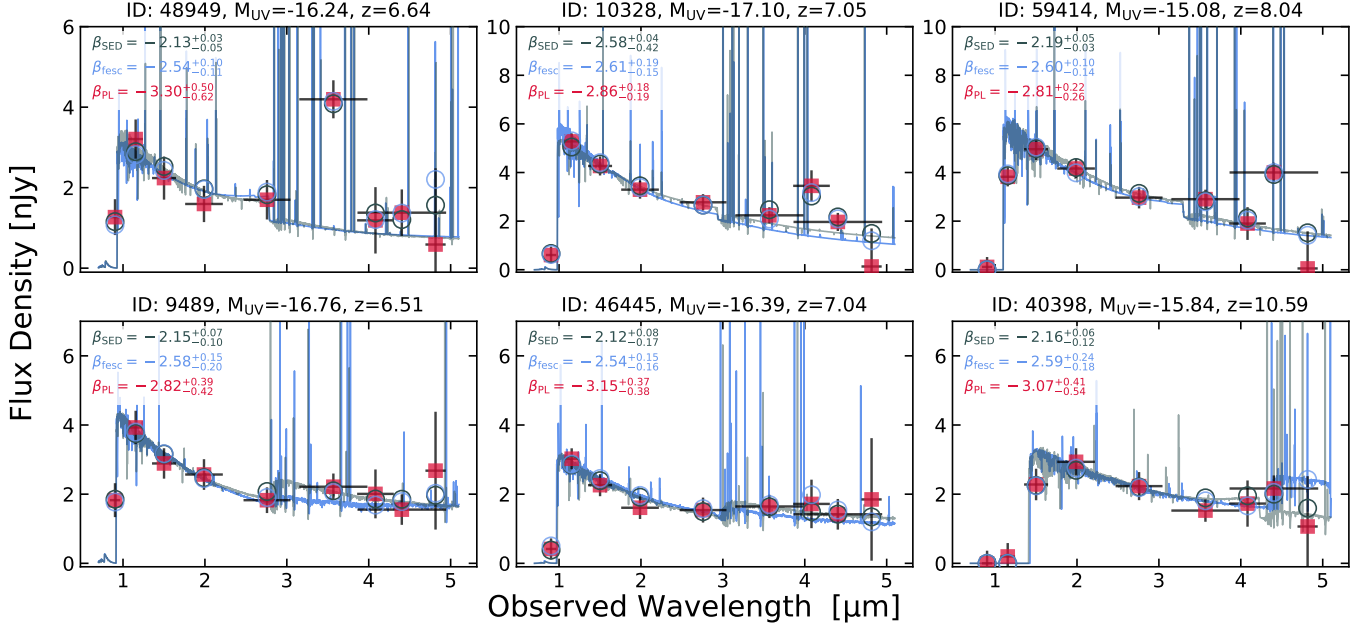


Figure 6. Sample of galaxies with the most robust extremely blue UV slopes ($\beta \leq -2.8$) which would require no dust attenuation and nebular continuum. The observed photometry is plotted as red squares. Best-fit SEDs and model photometry from standard BAGPIPES model with $f_{\text{esc}}=0$ are shown in gray. Adapted Giovinazzo et al. (2025) models with varying f_{esc} are shown in blue. We list the UV slope calculated directly from photometry (β_{PL}), the $f_{\text{esc}}=0$ SED (β_{SED}), and the varying f_{esc} SED (β_{fesc}).

scopic observations highlight the diversity of very blue GLIMPSE galaxies. While there is not a large population of extremely blue galaxies in GLIMPSE, there are a handful of very blue galaxies with weak nebular emission lines. If these galaxies are still producing ionizing photons, they must have significant f_{esc} and would be important for cosmic reionization. See Asada et al. (in preparation) for spectroscopy of such a GLIMPSE-*D* source.

5.3. Escape Fractions

Constraining the escape fractions of galaxies in the EoR is notoriously challenging, yet essential for identifying the sources responsible for reionization. At $z > 4$ direct detections of LyC are improbable, so f_{esc} is usually estimated through indirect tracers calibrated in the local universe. The gold standard for estimating f_{esc} is a multivariate predictor combining information on dust attenuation, nebular properties, and ionization state (Saldana-Lopez et al. 2022; Jaskot et al. 2024b; Mascia et al. 2024). Since the UV continuum slope traces both the dust and gas content of a galaxy, it is a powerful single variable predictor of f_{esc} (Chisholm et al. 2022), especially for populations of faint galaxies at high redshift where additional indirect indicators are observationally infeasible.

To contextualize whether our UV slopes are indeed correlated with f_{esc} , we analyze the relations between

β , A_V , $\text{H}\alpha$ emission, and M_{UV} for the photometrically selected $z \sim 6.3$ sample where $\text{H}\alpha$ is covered by the F480M filter. The left panel of Figure 8 shows rest-frame $\text{EW}(\text{H}\alpha)$ versus β , with points colored by their best-fit A_V from the standard BAGPIPES model. The strong correlation between β and A_V emphasizes that the UV slope primarily traces dust attenuation. We overlay the constant star-formation rate stellar population synthesis models with $f_{\text{esc}}=0$ and $f_{\text{esc}}=0.5$ from Zackrisson et al. (2013), adding dust attenuation to the zero f_{esc} model. As shown by the pink curve, the UV slope evolves minimally with age, reddening by $\Delta\beta \sim 0.5$ over 100 Myr. From the observed $\text{H}\alpha$ luminosities, we estimate the dust-corrected ξ_{ion} , noting these represent lower limits because any escaping LyC would reduce $\text{H}\alpha$ emission and thus lead to an underestimation of the intrinsic ξ_{ion} . The right panel of Figure 8 shows ξ_{ion} versus β , now colored according to M_{UV} .

We do not find a simple correlation between β and $\text{H}\alpha$ or ξ_{ion} ; instead, the trend is complicated by stellar population age and f_{esc} . Galaxies with the largest $\text{H}\alpha$ EW ($\log_{10} \text{EW}(\text{H}\alpha) \sim 3.5 \text{ \AA}$) have moderately red UV slopes ($\beta \sim -2.0$), requiring low escape fractions because ionizing photons must be absorbed to power Balmer emission and nebular continuum. These galaxies lie above the $f_{\text{esc}}=0$ model in the upper-right corner of the left panel of Figure 8 and tend to be slightly fainter than

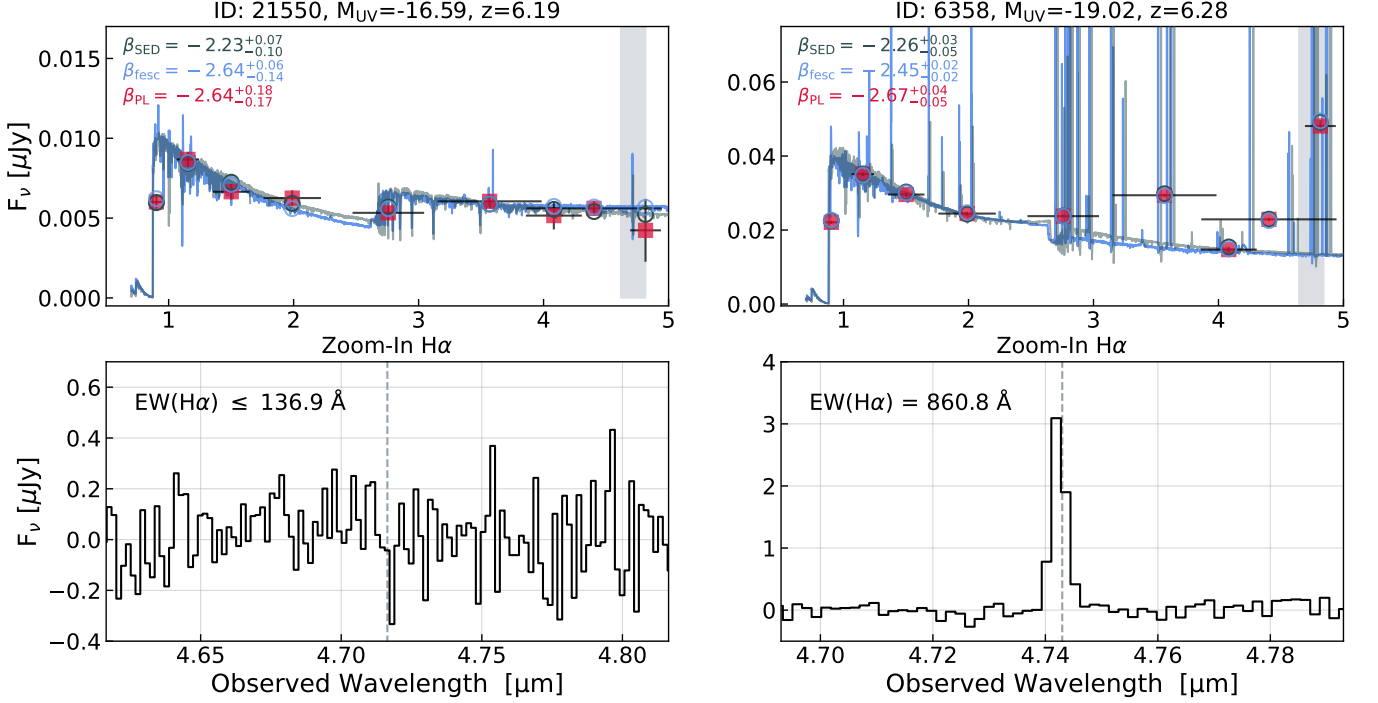


Figure 7. Two galaxies with blue UV slopes ($\beta \sim -2.6$) for which we have NIRSpec/MSA G395M coverage. In the top row, we show their observed photometry (red squares) and best-fit SEDs, same as in Figure 6. In the bottom row, we show the corresponding observed spectra near H α (gray shaded region), and report the equivalent width or upper limit, if undetected.

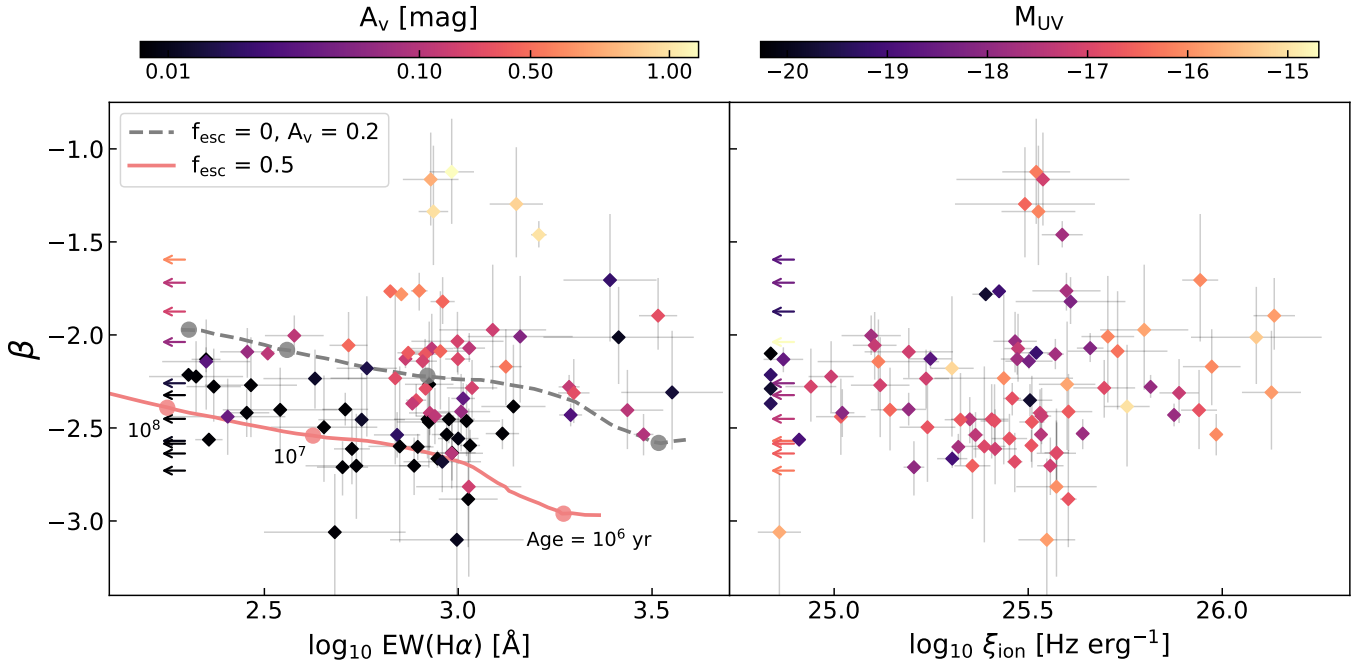


Figure 8. The relation between UV slope, rest-frame H α EW, ξ_{ion} , A_V , age, f_{esc} , and M_{UV} for the $z \sim 6.3$ photometrically selected sample where H α falls into the F480M filter. **Left:** β as a function of H α EW, coloring each point according to A_V . We show two stellar population synthesis models from Zackrisson et al. (2013): the $f_{\text{esc}}=0$, $A_V=0.2$ model (dashed gray curve) for which points above require zero LyC escape with increasing dust attenuation and the $f_{\text{esc}}=0.5$ model with no dust (pink curve) for which points below likely have nonzero f_{esc} . **Right:** β as a function of ξ_{ion} , where points are colored according to M_{UV} . We do not observe a significant trend between β and ξ_{ion} .

the full sample. In contrast, galaxies with the bluest UV slopes do not exhibit large ξ_{ion} values. In particular, no galaxy with $\beta \leq -2.5$ has H α equivalent width above 1075 Å, placing them below the $f_{\text{esc}}=0.5$ model and suggesting partial LyC leakage. Overall, we see that galaxies with red UV slopes have signatures of low f_{esc} from their strong nebular emission lines, while galaxies with blue UV slopes have rest-frame optical emission line properties that are consistent with non-zero f_{esc} .

As this subsample is photo-z selected, it is biased towards galaxies with strong emission. Chisholm et al. (in preparation) demonstrate that our faintest galaxies are preferentially observed during a burst of star-formation with elevated ξ_{ion} . This suggests we may be missing a subset of faint galaxies with no recent star-formation that would occupy the leftmost region of Figure 8. However, their older stellar population ages and the overall red UV slopes of the faint galaxies in the Lyman-break sample imply this population is unlikely to be significantly contributing to reionization.

In general, this multivariate analysis supports the interpretation that UV continuum slopes trace LyC escape at high redshift and faint magnitudes. Thus, we estimate the escape fraction for all galaxies in our sample using the $\beta-f_{\text{esc}}$ relation derived from local galaxies by Chisholm et al. (2022), capping f_{esc} at unity. As there is significant scatter in the empirical relation, this approach is best suited for estimating population-level trends rather than accurate measurements of f_{esc} for individual galaxies. To estimate uncertainties, we perturb β and the $\beta-f_{\text{esc}}$ fit parameters within their respective errors and recompute f_{esc} for 1000 iterations, adopting the inner 68th percentile of the resulting f_{esc} distribution as the uncertainty.

Figure 9 shows f_{esc} as a function of absolute magnitude, again showing the faint galaxies detected by GLIMPSE (blue circles) alongside the brighter JADES photometric sample (gray circles; Endsley et al. 2024). We calculate the mean f_{esc} in bins of M_{UV} for robust galaxies with $\text{S/N} \geq 5$ (red diamonds) following the procedure of Section 4, now using the average instead of median. We list the bin values in Table 4. The large scatter in predicted f_{esc} at all magnitudes results in the large binned error values.

We find that the faintest galaxies ($M_{\text{UV}} > -16$) do not have the highest escape fractions, but are, at best, consistent with brighter galaxies – as indicated by their UV continuum slopes. For comparison, we show the inferred evolution of f_{esc} with M_{UV} by applying the $\beta-f_{\text{esc}}$ relation to the Zhao & Furlanetto (2024) β – M_{UV} trend extrapolated towards fainter galaxies (yellow curves). These extrapolations agree with the $z > 6$ predictions

of Chisholm et al. (2022) and predicted that the faint galaxies observed with GLIMPSE would have near unity escape fractions which require extremely blue UV slopes ($\beta \sim -3.0$). Instead, the extrapolation overpredicts by more than 1σ the escape fraction of the majority of our faintest galaxies.

Once again, we fit all robust $\text{S/N} \geq 5$ GLIMPSE+JADES sources with both a SDPL and a single power-law ($\chi^2_{\text{red,SDPL}} \sim 22.2$, $\chi^2_{\text{red,PL}} \sim 31.1$), finding the SDPL with the following parameters to be the best fit: $\beta_0 = 0.39 \pm 0.94$, $M^* = -16.2 \pm 2.2$, $n = 0.91 \pm 2.9$, $\alpha_1 = 0.48 \pm 0.44$, and $\alpha_2 = -0.51 \pm 2.01$. These values indicate the escape fraction peaks at $\sim 20\%$ for galaxies with $M_{\text{UV}} \sim -16$ and declines sharply for fainter galaxies. Although the data is best-fit by a SDPL (solid red curve), we note that our mean f_{esc} bins are consistent with a constant $\sim 14\%$ escape fraction across all magnitudes (dashed red line), in agreement with findings of Giovinazzo et al. (2025) from SED-fitting and Mascia et al. (2024) from multivariate predictors but higher than the SED-inferred f_{esc} of Papovich et al. (2025).

This work provides the first population-level estimations for the expected escape fractions of galaxies with $M_{\text{UV}} > -16$, although not without caveats. The observed, low-z $\beta-f_{\text{esc}}$ relation shows roughly an order of magnitude scatter in f_{esc} at fixed UV slope, leading to large uncertainties on f_{esc} for individual galaxies. Nevertheless, the overall trend suggests that the faintest galaxies, in general, have escape fractions comparable to the full sample. In addition, we have assumed the $\beta-f_{\text{esc}}$ relation measured from local galaxies with $\beta > -2.6$ extends to higher redshifts, fainter magnitudes, and bluer galaxies. Encouragingly, initial evidence shows this relation agrees with other multivariate estimates of f_{esc} at high redshift (Gazagnes et al. 2025). These f_{esc} predictions provide the first empirically constrained estimates of the escape fractions of the faintest galaxies, offering a direct look at their role in reionization.

Table 4. Mean f_{esc} for the four M_{UV} bins shown in Figure 9. Same magnitude bins as Table 3.

Magnitude bin	M_{UV}	$\langle f_{\text{esc}} \rangle$
$-21 \leq M_{\text{UV}} < -19$	-19.6 ± 0.23	$0.08^{+0.09}_{-0.04}$
$-19 \leq M_{\text{UV}} < -17$	-17.9 ± 0.27	$0.14^{+0.21}_{-0.07}$
$-17 \leq M_{\text{UV}} < -15$	-16.5 ± 0.25	$0.18^{+0.26}_{-0.07}$
$-15 \leq M_{\text{UV}} < -13$	-14.4 ± 0.28	$0.11^{+0.20}_{-0.06}$

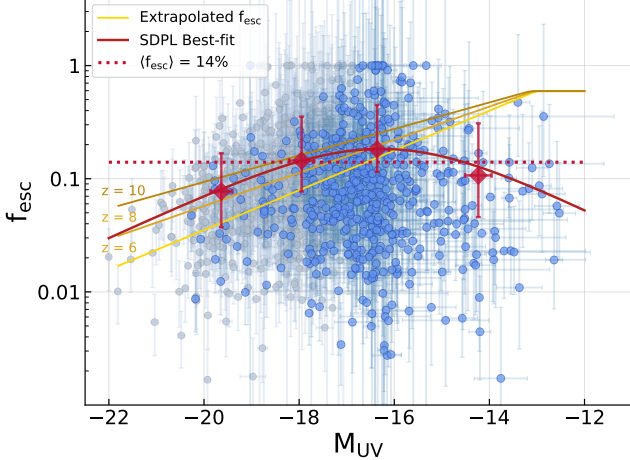


Figure 9. The modest escape fractions of the faintest galaxies now observable with GLIMPSE (blue circles) alongside the brighter JADES sample (gray circles). Red diamonds are mean f_{esc} for equal-width M_{UV} bins of robust galaxies with $S/N \geq 5$ and the solid red curve is best-fitting relation to all robust galaxies. We compare to the commonly used prediction from applying the local β - f_{esc} relation on the UV slopes of Zhao & Furlanetto (2024), extrapolated to fainter magnitudes at three redshifts (yellow curves).

5.4. Comparison of Faint Galaxies to Simulations

As discussed above, the faintest galaxies observed with GLIMPSE ($M_{\text{UV}} \sim -14$) are a diverse sample, but few exhibit the extremely blue UV slopes and high escape fractions often assumed for faint galaxies in the EoR. To investigate whether this is consistent with simulations, we compare our results to the mock JWST observations of MEGATRON (Katz et al. 2025b), a cosmological simulation with on-the-fly radiative transport that self-consistently models faint, high- z galaxies with sub-parsec resolution.

To enable a direct comparison, we construct a mock sample of simulated galaxies broadly matched to the M_{UV} distribution of our observed GLIMPSE sample. We bin GLIMPSE galaxies into 10 equal-width M_{UV} intervals. From each M_{UV} range, we randomly draw twice the number of simulated galaxies as observed with GLIMPSE, to sample a sufficient number of faint galaxies. The resulting mock sample spans a higher redshift range of $8 < z < 20$, with a median redshift of $\langle z_M \rangle \sim 10.3$ compared to GLIMPSE ($\langle z_G \rangle \sim 6.7$). Both populations show minimal evolution in β with redshift, justifying the comparison across redshift ranges.

In the left panel of Figure 10, we compare the MEGATRON UV slopes (scatter points) to those observed in GLIMPSE (blue contours). The faint simulated galaxies show slightly redder UV slopes and a broader dispersion than their brighter counterparts. GLIMPSE galaxies

are, on average, redder than simulated ($\langle \beta_G \rangle \sim -2.28$, $\langle \beta_M \rangle \sim -2.49$), reflecting increased dust attenuation. We observe a much wider range of β values, likely enhanced by photometric scatter, but underscoring the diversity of age and dust properties of the observed galaxies. Both observed and simulated galaxies display a wide range of $\text{H}\alpha$ EWs across all magnitudes (color-coding of points in left panel of Figure 10), reinforcing that faint, high-redshift galaxies can be actively star-forming or quiescent. Notably, the majority of faint galaxies in MEGATRON exhibit low ionizing photon output ($\langle f_{\text{esc}} \times \xi_{\text{ion}} \rangle$), but for two distinct reasons.

The first subset of faint simulated galaxies have low escape fractions, strong $\text{H}\alpha$ emission, and relatively red UV slopes for such high redshift galaxies ($\beta \sim -2.4$). These are the orange points on the left panel of Figure 10. Among the 75 galaxies in our mock sample with $M_{\text{UV}} > -16$ and $\text{H}\alpha$ EW $\geq 1500\text{\AA}$, the average escape fraction is below 0.1%, as emphasized by the histogram of the right panel. As discussed in Section 5.1, we observe a comparable population in GLIMPSE (faint galaxies with moderately red UV slopes and strong $\text{H}\alpha$ emission) suggestive of vigorously star-forming galaxies with UV slopes dominated by nebular continuum or reddened by dust attenuation. These galaxies lie in the upper-right corner of the β -EW($\text{H}\alpha$) plot in the left panel of Figure 8. The escape fractions predicted by MEGATRON for these galaxies support the interpretation that extreme nebular line-emission in faint, red galaxies requires low LyC escape fractions.

In addition, we also identify faint MEGATRON galaxies with low ionizing photon output due to old stellar populations. The reddest UV slopes in our mock sample are from galaxies with evolved stellar populations which age toward fainter magnitudes and reduced $\text{H}\alpha$ emission, similar to the GLIMPSE galaxies shown in the middle column of Figure 5 and those in the $z \sim 6.3$ photometrically selected sample with upper limits on their $\text{H}\alpha$ emission (arrows in Figure 8). Although these galaxies have high f_{esc} reported from MEGATRON, they no longer host the young, massive stars capable of producing ionizing photons and thus have a negligible contribution to reionization.

Lastly, we do find evidence in MEGATRON for a subset of faint galaxies that contribute non-negligibly to reionization. The faint galaxies with the bluest UV slopes ($\beta < -2.6$) show weakened nebular emission ($\langle \text{EW H}\alpha \rangle = 427\text{\AA}$) due to their relatively high escape fractions ($\langle f_{\text{esc}} \rangle = 28.9\%$). However, these blue and high f_{esc} galaxies comprise only $\sim 16\%$ of all galaxies fainter than $M_{\text{UV}} = -16$ in the mock sample, indicating that high LyC leakage is not common among

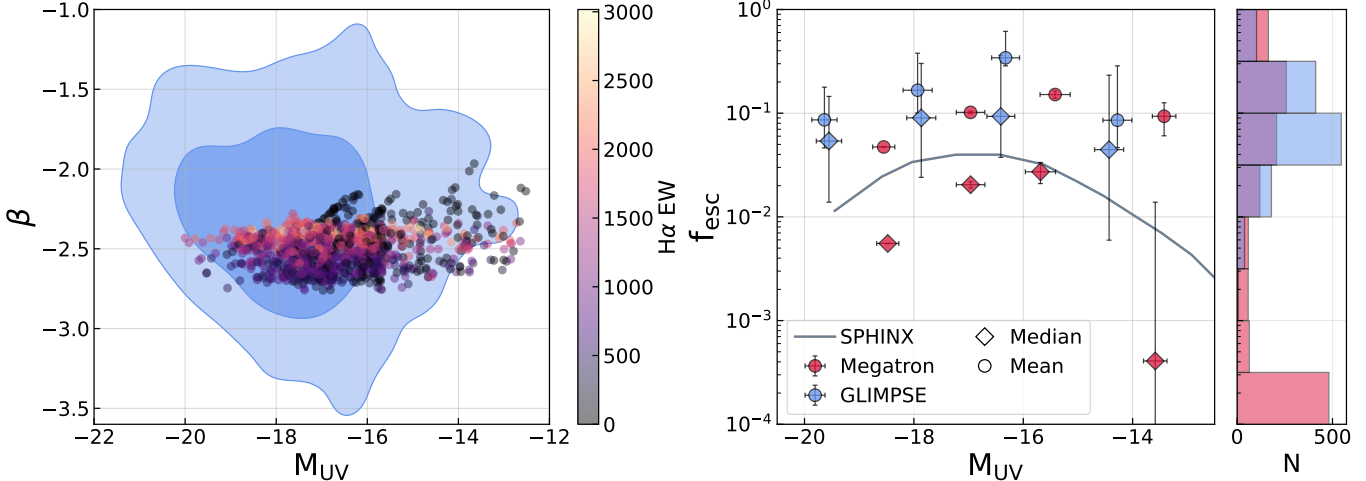


Figure 10. Comparison of faint galaxies from the MEGATRON simulation (Katz et al. 2025b) to GLIMPSE galaxies. **Left:** UV slope versus M_{UV} for simulated galaxies colored according $H\alpha$ EW. Blue contours enclose the 68th and 95th percentiles of GLIMPSE galaxies in Figure 4. **Right:** LyC escape fraction for equal-width bins of M_{UV} for MEGATRON (red points) and GLIMPSE (blue points). As the f_{esc} distribution is significantly skewed, we plot both the median (diamonds) and mean (circles) f_{esc} and show its distribution on the right axis. We additionally over-plot the $z=6-7$ mean f_{esc} from the SPHINX simulations (Rosdahl et al. 2022).

the faintest galaxies. We similarly observe few faint GLIMPSE galaxies with blue UV slopes and low $H\alpha$ emission needed for high f_{esc} .

Overall, the majority of faint galaxies in the MEGATRON sample do not have high escape fractions, in agreement with our results for faint GLIMPSE galaxies. As shown by the histogram in the right panel of Figure 10, the distribution of simulated f_{esc} is strongly skewed, with a long tail towards low values and a pileup at zero f_{esc} . As such, we plot both the MEGATRON median (red diamonds) and mean (red circles) escape fractions in equal-width bins of M_{UV} . In the faintest bin, 53.8% of simulated galaxies have $f_{esc} < 0.1\%$, compared to only $\sim 37\%$ in the brighter bins. As with GLIMPSE galaxies, both the median and mean escape fractions decrease towards the faintest bin.

Additionally, we plot the mean escape fractions from the SPHINX simulation at $z=6-7$ (Rosdahl et al. 2022) as the solid gray line in the right panel of Figure 10. The predicted mean escape fraction peaks at $M_{UV} \sim -17$, before sharply decreasing towards fainter galaxies. Rosdahl et al. (2022) attribute this peak to the mass range that is low enough for stellar feedback to remain effective, yet high enough for clustered star formation to produce concentrated supernovae which clear channels for LyC escape.

In general, the escape fractions calculated in MEGATRON and SPHINX simulations agree with our estimated $\langle f_{esc} \rangle$ for the faint galaxies observed with GLIMPSE. This suggests that the faintest galaxies may

not have the highest f_{esc} , providing crucial constraints for cosmic reionization.

5.5. Cosmic Reionization with GLIMPSE

Many studies suggest the faintest galaxies are the primary drivers of cosmic reionization due to their theoretically high number densities, large ionizing efficiencies, and high escape fractions as extrapolated from lower redshift studies of brighter galaxies. However, it is only recently with JWST that we are able to directly observe these faint galaxies in the EoR, and only with ultra-deep imaging of strongly lensed fields that we can observe statistical samples of the faintest galaxies. As such, we analyze what GLIMPSE observations of these faint, high- z galaxies imply about the progression and drivers of reionization.

We run the simple reionization model of Muñoz et al. (2024) which solves for the volume-averaged neutral and ionized hydrogen fractions by integrating over the number density of ionizing photons from star-forming galaxies ($\dot{n}_{ion} = \int dM_{UV} \Phi_{UV} \dot{N}_{ion} f_{esc}$). We use a clumping factor of $C = 3$ and integrate down to a cutoff magnitude of $M_{UV}^{ion, cutoff} = -12$, the faintest GLIMPSE galaxy. The estimated ionizing photons of GLIMPSE galaxies and its evolution with time must balance recombinations in the IGM to match independent observational constraints on the CMB optical depth (Planck Collaboration et al. 2016) and neutral hydrogen fraction ($x_{HI}(z)$) (Mason et al. 2025).

In Figure 11, we test how well various reionization histories compare to these observational constraints. The

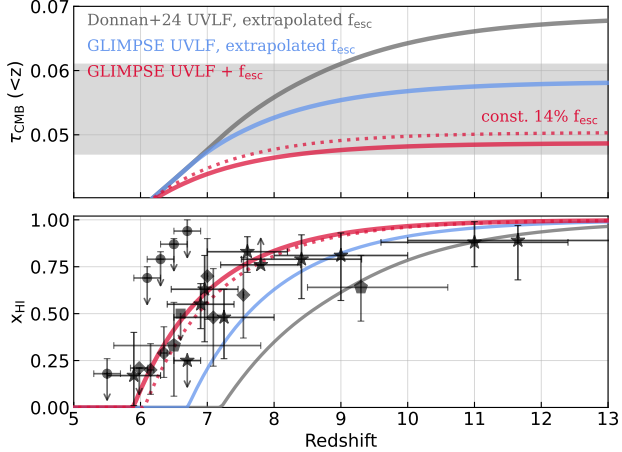


Figure 11. Cosmic reionization as observed with GLIMPSE (red lines) agrees with constraints on CMB optical depth (gray shaded region, top; Planck Collaboration et al. 2016) and neutral hydrogen fraction (x_{HI}) evolution with redshift (bottom; Mason et al. 2025). The gray line uses the UVLF of Donnan et al. (2024) at $z > 9$ and Bouwens et al. (2021) at $z \leq 9$, while red and blue lines use that of Chemerynska et al. (2025). The gray and blue lines use the f_{esc} prescription based on the UV slopes of Zhao & Furlanetto (2024) extrapolated to fainter galaxies (yellow lines in Figure 9), based on the low- z f_{esc} used in Muñoz et al. (2024). Solid and dotted red lines use GLIMPSE SDPL and constant 14% $f_{\text{esc}}(\text{M}_{\text{UV}}, z)$, respectively. All models use ξ_{ion} from Simmonds et al. (2024). Code implementing this reionization model is available at <https://github.com/JulianBMunoz/Simple-Reionization-Plot>.

gray curve adopts the UVLF of Donnan et al. (2024) at $z > 9$ and Bouwens et al. (2021) at $z \leq 9$. The red and blue curves instead use the Chemerynska et al. (2025) double power-law UVLF fit to the $z > 8$ GLIMPSE galaxies in our sample, evolving only the normalization with redshift as the slope and M_{\star} remain relatively constant. Both the gray and blue curves adopt the extrapolated $f_{\text{esc}}(\text{M}_{\text{UV}}, z)$ relation shown in Figure 9. The red curves show results using escape fraction prescriptions in agreement with GLIMPSE observations: the solid line uses the SDPL $f_{\text{esc}}(\text{M}_{\text{UV}})$ fit, while the dotted line assumes a constant $f_{\text{esc}} = 14\%$ for all M_{UV} . All models use the $z \sim 6.5$ $\xi_{\text{ion}}(\text{M}_{\text{UV}})$ from the mass-complete sample of Simmonds et al. (2024) which finds a modest redshift and M_{UV} evolution with $\log(\xi_{\text{ion}}) \simeq 25.4$. This relation agrees with the ξ_{ion} measurements calculated from the completeness-corrected $z \sim 6.3$ GLIMPSE photometrically selected sample from Chisholm et al. (in prep.). The red curves therefore represent a self-consistent model in which ionizing parameters are directly informed by GLIMPSE observations of the faint galaxies in this sample.

The difference between the blue and gray curves arises from the ~ 0.5 dex lower normalization of the Chemerynska et al. (2025) UVLF compared to that of Donnan et al. (2024), as both have faint-end slopes of $\alpha \simeq -2.1$. Although the individual measurements of Donnan et al. (2024) are consistent with the Chemerynska et al. (2025) fit within uncertainties, the Donnan et al. (2024) extrapolated fit across redshift overpredicts the number of faint galaxies compared to GLIMPSE. Thus, the GLIMPSE UVLF predicts fewer faint galaxies at high redshift, resulting in a midpoint of reionization that happens at a $\Delta z \sim 0.5$ later in cosmic time.

The offset of the red curves from the blue is driven by the lower average f_{esc} inferred here for faint galaxies in GLIMPSE compared to previous extrapolations. The GLIMPSE SDPL fit predicts faint galaxies have a factor of 3 lower f_{esc} than previous predictions, slowing reionization by an additional $\Delta z \sim 0.75$ later in cosmic time. While the SDPL is the best-fit to robust GLIMPSE+JADES data, a constant $f_{\text{esc}} = 14\%$ remains plausible given the uncertainties, and the prediction reionization history is shown by the dotted red line. We find that adopting the SDPL versus the constant f_{esc} only marginally changes the reionization history.

The solid red line represents the reionization history informed by GLIMPSE observations of the faintest galaxies. This model agrees with the lower-end CMB optical depth constraint and nearly all Lyman- α forest x_{HI} constraints (Mason et al. 2025), unlike the blue and gray curves which use f_{esc} prescriptions extrapolated from brighter galaxies. The GLIMPSE model predicts reionization is halfway complete ($x_{\text{HI}} = 0.5$) at $z \sim 6.7$ with a late ending of reionization (Bosman et al. 2022; Becker et al. 2021). The moderation of the reionization history largely arises from the GLIMPSE observations of the faintest galaxies that suggest modest f_{esc} and ξ_{ion} , reducing \dot{n}_{ion} and slowing reionization to match $x_{\text{HI}}(z)$ observations. These results resolve the ionizing photon budget tension of Muñoz et al. (2024) while still integrating down to feasible faint-end cutoff of -12 .

Finally, in Figure 12 we determine what these updated Φ_{UV} , ξ_{ion} , and f_{esc} prescriptions suggest about which galaxies were the drivers of reionization. We calculate the total ionizing photon contribution to reionization by integrating over the GLIMPSE $\Phi_{\text{UV}} \times f_{\text{esc}} \times \xi_{\text{ion}} \times L_{\text{UV}}$ and normalizing over our sample brightness range ($\text{M}_{\text{UV}} \in [-22, -12]$). The red solid and dashed lines use GLIMPSE-calibrated prescriptions from the corresponding reionization models of Figure 11. The GLIMPSE SDPL f_{esc} relation (solid line) peaks near $\text{M}_{\text{UV}} \sim -16$ and drops off in both directions. While the steep UVLF does rise for fainter galaxies (faint-end

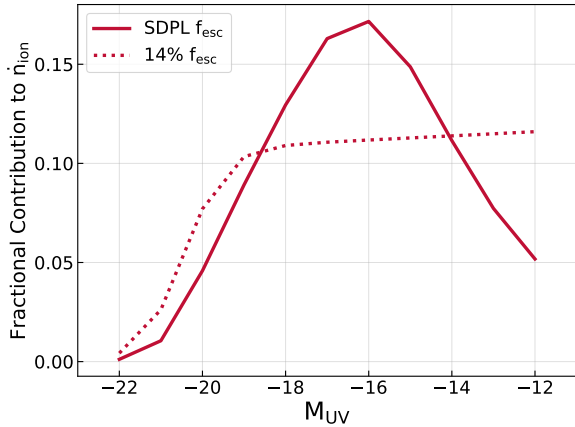


Figure 12. The contribution of ionizing photons to reionization as a function of M_{UV} , normalized by the total ionizing photon budget over observed GLIMPSE galaxies ($\int_{-22}^{-12} \Phi_{\text{UV}} \xi_{\text{ion}} f_{\text{esc}} \text{L}_{\text{UV}} dM_{\text{UV}}$). Both lines use GLIMPSE inputs of the corresponding models in Figure 11. The solid line uses the best-fit SDPL fit to $f_{\text{esc}}(M_{\text{UV}})$ shown in Figure 9, predicting moderately faint galaxies with $M_{\text{UV}} \sim -16$ are the drivers of reionization. The dashed line uses a constant 14% f_{esc} , consistent with GLIMPSE findings.

slope $\alpha = -2.1$), it does not rise fast enough to compensate for f_{esc} and ξ_{ion} decreasing. This implies that galaxies with M_{UV} between -18 and -14 mag were the drivers of cosmic reionization, a result consistent with the GLIMPSE O III + H β LF (Korber et al. 2025) and slightly fainter than predicted in Matthee et al. (2022). The SDPL relation places the first, second, and third quartiles of the cumulative \dot{n}_{ion} distribution at $M_{\text{UV}} \simeq -18.2$, -16.6 , and -15 , respectively, reinforcing that intermediate-luminosity systems produced the majority of ionizing photons. However, our large uncertainties on the f_{esc} of faint galaxies result in $f_{\text{esc}}(M_{\text{UV}})$ also being consistent with a flat $\sim 14\%$ f_{esc} . Shown as the dotted line in Figure 12, this constant f_{esc} results in all galaxies in the faint-end of the UVLF ($M_{\text{UV}} \geq -18$) contributing similar amount of ionizing photons to cosmic reionization.

GLIMPSE observations suggest galaxies around $M_{\text{UV}} \sim -16$ are the prominent drivers of cosmic reionization, with galaxies fainter than $M_{\text{UV}} \sim -14$ contributing only slightly or equally, at best. The surprising red UV slopes of faint GLIMPSE galaxies suggest a turnover in their f_{esc} below $M_{\text{UV}} \sim -16$ resulting in a natural cutoff in the ionizing photon production where galaxies fainter than $M_{\text{UV}} \sim -12$ do not significantly contribute to reionization.

6. CONCLUSIONS

Leveraging data from the ultra-deep, gravitationally lensed *JWST*/NIRCam GLIMPSE survey, we present the first statistical sample of UV continuum slopes of the faintest galaxies in the EoR. This sample covers photometric redshifts of $z = 6$ -16 and reaches absolute magnitudes down to $M_{\text{UV}} = -12$, finding a total of 138 galaxies with $M_{\text{UV}} > -16$. We estimate UV slopes by power-law fitting directly to filters in the rest-frame UV. We analyze UV slopes in combination with rest-optical emission from NIRCam medium-band filters to characterize faint galaxies, evaluate extremely blue UV slopes, and ultimately estimate LyC escape fractions to better understand cosmic reionization. We summarize our main findings below.

1. We find no statistically significant decrease in β with redshift. We calculate $d\beta/dz = -0.047 \pm 0.014$, consistent with Topping et al. (2024); Roberts-Borsani et al. (2024) but shallower than Cullen et al. (2024); Austin et al. (2024). We find minimal difference in the redshift evolution of β at fixed M_{UV} .
2. The faintest galaxies ($M_{\text{UV}} \gtrsim -16$) do not have the bluest UV slopes and are, at best, consistent with brighter galaxies. Our UV slopes of brighter ($M_{\text{UV}} \sim -18$) galaxies agree with the best-fit trends of Cullen et al. (2023); Topping et al. (2024), but extrapolating these trends towards fainter galaxies predicts much bluer slopes than observed with GLIMPSE. We find a large variance in observed β values across all M_{UV} .
3. We observe a diverse population of faint galaxies which includes dusty galaxies, older stellar populations, and low-mass star-forming galaxies. We find evidence for strong dust attenuation in low-mass galaxies as early as $z \sim 6.5$. In general, galaxies with $M_{\text{UV}} \gtrsim -16$ are not a monolithic population.
4. We do not find convincing evidence for a population of galaxies with extremely blue UV slopes, even with the increased depth of GLIMPSE. Of the 52 galaxies with $\beta \leq -2.8$, most lie near the detection threshold and can be explained by photometric scatter. We classify only 6 galaxies as having more robust extreme β values, but spectroscopy is needed to verify.
5. We analyze the relation between β , H α EW, f_{esc} , and A_{V} for the $z \sim 6.3$ photometrically selected subsample where F480M covers H α . We see that galaxies with red UV slopes typically have high dust attenuation and/or strong H α emission, indicating low LyC escape fractions. In comparison,

galaxies with blue UV slopes require low dust attenuation and do not have the highest H α EW, consistent with higher escape fractions. We find similar behavior in the MEGATRON simulation, where faint galaxies have slightly redder UV slopes and low average ionizing output, justifying using the UV slope to estimate average f_{esc} for populations of faint galaxies at high redshifts.

6. The faintest galaxies do not have the highest escape fractions, as estimated from the β - f_{esc} relation of Chisholm et al. (2022). We find that $f_{\text{esc}}(\text{M}_{\text{UV}})$ is consistent with a constant mean $\sim 14\% f_{\text{esc}}$, but best-fit by a smooth double power-law which peaks at $f_{\text{esc}} \sim 20\%$ at $\text{M}_{\text{UV}} = -16.25$ and decreases for fainter galaxies.
7. We run the simple reionization model of Muñoz et al. (2024) using the GLIMPSE UVLF of Chemerynska et al. (2025), the ξ_{ion} distribution of Simmonds et al. (2024) which is consistent with GLIMPSE findings (Chisholm et al. in prep.), and f_{esc} from this work. These GLIMPSE observations of the ionizing properties of galaxies in the EoR produce a reionization history consistent with the CMB optical depth and Lyman- α forest constraints. Our best-fit f_{esc} results in galaxies between $\text{M}_{\text{UV}} \simeq -18$ and -14 contributing $\sim 60\%$ of the ionizing photons need to reionize the universe.

Estimating LyC escape fractions for faint galaxies in the EoR is notoriously difficult. In general, GLIMPSE observations suggest that the faintest galaxies are a diverse population which, as a whole, do not necessarily have the highest f_{esc} . This initial GLIMPSE into the

UV slopes of the faintest galaxies has provided a nuanced view of cosmic reionization and has provided new benchmarks for understanding the sources responsible.

ACKNOWLEDGMENTS

We thank the referee for the insightful comments and suggestions that improved the clarity of this work. This work is based on observations made with the NASA/ESA/CSA James Webb Space Telescope. The data were obtained from the Mikulski Archive for Space Telescopes at the Space Telescope Science Institute, which is operated by the Association of Universities for Research in Astronomy, Inc., under NASA contract NAS 5-03127 for JWST. These observations are associated with programs #3293 and #9233. Support for programs #3293 and #9233 was provided by NASA through a grant from the Space Telescope Science Institute, which is operated by the Association of Universities for Research in Astronomy, Inc., under NASA contract NAS 5-03127. This work has received funding from the Swiss State Secretariat for Education, Research and Innovation (SERI) under contract number MB22.00072, as well as from the Swiss National Science Foundation (SNSF) through project grant 200020_207349. The Cosmic Dawn Center (DAWN) is funded by the Danish National Research Foundation under grant DNRF140. AA acknowledges support by the Swedish research council Vetenskapsrådet (VR) project 2021-05559, and VR consolidator grant 2024-02061. The Dunlap Institute is funded through an endowment established by the David Dunlap family and the University of Toronto. We acknowledge the support of the Canadian Space Agency (CSA) [25JWGO4A06].

REFERENCES

Table 5. The GLIMPSE sample and derived properties used in this work.

ID	RA	Dec.	μ	M_{UV}	z_{phot}	β_{PL}	$\beta_{\text{PL,16th}}$	$\beta_{\text{PL,84th}}$	β_{SED}	$\beta_{\text{SED,16th}}$	$\beta_{\text{SED,84th}}$	β_{fesc}	$\beta_{\text{fesc,16th}}$	$\beta_{\text{fesc,84th}}$	A_{V}
9948	342.19	-44.55	1.78	-16.30 \pm 1.41	6.80 \pm 0.27	-2.07	-2.40	-1.74	-2.04	-2.24	-2.08	-2.29	-2.34	-2.10	0.23
10400	342.18	-44.55	2.18	-16.21 \pm 0.03	6.84 \pm 0.64	-1.16	-2.17	-0.96	-1.95	-2.15	-2.04	-2.18	-2.27	-1.97	0.23
12380	342.18	-44.55	2.84	-15.43 \pm 0.10	6.43 \pm 0.23	-2.46	-2.91	-2.01	-2.32	-2.30	-2.06	-2.31	-2.48	-2.10	0.00
12786	342.18	-44.55	2.78	-15.56 \pm 0.12	7.22 \pm 0.26	-2.28	-3.25	-2.06	-2.16	-2.24	-2.09	-2.34	-2.49	-2.10	0.00
16257	342.18	-44.54	4.35	-15.50 \pm 0.10	7.75 \pm 0.32	-1.80	-2.04	-1.56	-2.02	-2.14	-1.97	-1.99	-2.13	-1.97	0.00
16271	342.18	-44.54	3.95	-15.22 \pm 0.52	6.68 \pm 0.36	-1.43	-2.05	-0.87	-2.10	-2.17	-2.07	-1.89	-2.32	-1.95	0.00
17876	342.18	-44.51	1.96	-16.54 \pm 0.09	6.56 \pm 0.21	-2.11	-2.44	-1.78	-2.01	-2.14	-1.97	-2.18	-2.23	-1.99	0.00
19355	342.17	-44.53	12.41	-13.89 \pm 0.10	6.60 \pm 0.26	-1.98	-2.44	-1.50	-2.12	-2.21	-2.09	-2.33	-2.37	-2.08	0.00
19881	342.21	-44.53	4.95	-15.02 \pm 0.52	6.58 \pm 0.19	-1.91	-2.30	-1.52	-2.18	-2.27	-2.10	-2.41	-2.42	-2.09	0.06
20025	342.21	-44.53	3.38	-16.37 \pm 0.08	6.62 \pm 0.11	-2.27	-2.46	-2.10	-1.91	-2.08	-1.93	-2.02	-2.20	-2.01	0.00
20026	342.21	-44.53	3.34	-16.45 \pm 0.06	6.39 \pm 0.08	-2.20	-2.34	-2.07	-1.92	-2.00	-1.87	-2.07	-2.13	-2.01	0.00
20891	342.19	-44.53	3.53	-16.35 \pm 0.56	6.63 \pm 0.54	-3.34	-3.78	-1.75	-2.38	-2.31	-2.09	-2.66	-2.49	-2.08	0.00
23217	342.16	-44.53	3.03	-15.32 \pm 0.08	6.75 \pm 0.29	-2.13	-2.49	-1.71	-2.12	-2.17	-2.06	-1.91	-2.32	-1.99	0.00
23448	342.20	-44.53	34.16	-12.53 \pm 0.34	6.70 \pm 0.17	-2.12	-2.41	-1.79	-2.16	-2.14	-2.05	-2.15	-2.30	-2.02	0.00
24483	342.19	-44.53	13.14	-13.98 \pm 0.11	6.67 \pm 0.25	-2.23	-2.72	-1.56	-2.15	-2.17	-2.07	-2.11	-2.32	-2.01	0.01
24893	342.16	-44.53	3.40	-15.61 \pm 0.09	6.89 \pm 0.19	-1.91	-2.27	-1.62	-2.00	-2.17	-2.06	-2.14	-2.33	-2.05	0.00
26321	342.19	-44.53	12.86	-14.16 \pm 0.11	7.21 \pm 0.43	-1.97	-2.30	-1.12	-2.08	-2.20	-2.08	-1.93	-2.37	-1.98	0.03
26864	342.19	-44.53	12.77	-14.21 \pm 0.04	6.63 \pm 0.77	-1.51	-2.04	-1.20	-2.01	-2.16	-2.06	-1.89	-2.26	-1.95	0.13
27601	342.19	-44.53	15.16	-14.27 \pm 0.21	7.02 \pm 0.33	-1.82	-2.48	-1.49	-2.12	-2.21	-2.08	-2.30	-2.44	-2.14	0.00
29612	342.19	-44.53	24.74	-14.52 \pm 0.15	6.71 \pm 1.14	-2.08	-3.05	-0.86	-2.11	-2.16	-2.04	-1.94	-2.29	-1.96	0.00
31042	342.17	-44.53	6.55	-14.56 \pm 1.83	6.71 \pm 0.76	-1.71	-2.81	-1.72	-1.84	-2.23	-2.07	-1.98	-2.36	-2.04	0.29
32505	342.21	-44.53	2.85	-16.70 \pm 0.02	6.84 \pm 0.02	-2.49	-2.65	-2.34	-2.15	-2.17	-2.11	-2.40	-2.42	-2.31	0.01
33643	342.21	-44.53	2.67	-15.88 \pm 0.16	7.28 \pm 0.27	-3.07	-3.44	-2.39	-2.35	-2.36	-2.12	-2.67	-2.59	-2.18	0.00
34689	342.16	-44.53	19.03	-13.93 \pm 0.17	6.64 \pm 0.15	-1.83	-2.19	-1.46	-2.06	-2.16	-2.06	-2.26	-2.35	-2.07	0.02
35742	342.19	-44.54	20.15	-13.91 \pm 1.93	6.97 \pm 0.43	-1.78	-2.15	-1.55	-1.95	-2.21	-2.09	-2.03	-2.31	-2.06	0.31

NOTE—Only the first 25 rows are shown. Full table available online.

Bhatawdekar, R., & Conselice, C. J. 2021, *ApJ*, 909, 144, doi: [10.3847/1538-4357/abdd3f](https://doi.org/10.3847/1538-4357/abdd3f)

Bosman, S. E. I., Davies, F. B., Becker, G. D., et al. 2022, *MNRAS*, 514, 55, doi: [10.1093/mnras/stac1046](https://doi.org/10.1093/mnras/stac1046)

Bouwens, R. J., Illingworth, G. D., Oesch, P. A., et al. 2015a, *ApJ*, 811, 140, doi: [10.1088/0004-637X/811/2/140](https://doi.org/10.1088/0004-637X/811/2/140)

—. 2012, *ApJ*, 754, 83, doi: [10.1088/0004-637X/754/2/83](https://doi.org/10.1088/0004-637X/754/2/83)

—. 2014, *ApJ*, 793, 115, doi: [10.1088/0004-637X/793/2/115](https://doi.org/10.1088/0004-637X/793/2/115)

—. 2015b, *ApJ*, 803, 34, doi: [10.1088/0004-637X/803/1/34](https://doi.org/10.1088/0004-637X/803/1/34)

Bouwens, R. J., Oesch, P. A., Stefanon, M., et al. 2021, *AJ*, 162, 47, doi: [10.3847/1538-3881/abf83e](https://doi.org/10.3847/1538-3881/abf83e)

Calzetti, D., Armus, L., Bohlin, R. C., et al. 2000, *ApJ*, 533, 682, doi: [10.1086/308692](https://doi.org/10.1086/308692)

Calzetti, D., Kinney, A. L., & Storchi-Bergmann, T. 1994, *ApJ*, 429, 582, doi: [10.1086/174346](https://doi.org/10.1086/174346)

Carnall, A. C., McLure, R. J., Dunlop, J. S., & Davé, R. 2018, *MNRAS*, 480, 4379, doi: [10.1093/mnras/sty2169](https://doi.org/10.1093/mnras/sty2169)

Chemerynska, I., Atek, H., Furtak, L. J., et al. 2025, arXiv e-prints, arXiv:2509.24881, doi: [10.48550/arXiv.2509.24881](https://doi.org/10.48550/arXiv.2509.24881)

Chisholm, J., Prochaska, J. X., Schaefer, D., Gazagnes, S., & Henry, A. 2020, *MNRAS*, 498, 2554, doi: [10.1093/mnras/staa2470](https://doi.org/10.1093/mnras/staa2470)

Chisholm, J., Saldana-Lopez, A., Flury, S., et al. 2022, *MNRAS*, 517, 5104, doi: [10.1093/mnras/stac2874](https://doi.org/10.1093/mnras/stac2874)

Cullen, F., McLure, R. J., McLeod, D. J., et al. 2023, *MNRAS*, 520, 14, doi: [10.1093/mnras/stad073](https://doi.org/10.1093/mnras/stad073)

Cullen, F., McLeod, D. J., McLure, R. J., et al. 2024, *MNRAS*, 531, 997, doi: [10.1093/mnras/stae1211](https://doi.org/10.1093/mnras/stae1211)

Davies, F. B., Bosman, S. E. I., & Furlanetto, S. R. 2024, arXiv e-prints, arXiv:2406.18186, doi: [10.48550/arXiv.2406.18186](https://doi.org/10.48550/arXiv.2406.18186)

Donnan, C. T., McLeod, D. J., Dunlop, J. S., et al. 2023, *MNRAS*, 518, 6011, doi: [10.1093/mnras/stac3472](https://doi.org/10.1093/mnras/stac3472)

Donnan, C. T., McLure, R. J., Dunlop, J. S., et al. 2024, *MNRAS*, 533, 3222, doi: [10.1093/mnras/stae2037](https://doi.org/10.1093/mnras/stae2037)

Donnan, C. T., Dickinson, M., Taylor, A. J., et al. 2025, arXiv e-prints, arXiv:2507.10518, doi: [10.48550/arXiv.2507.10518](https://doi.org/10.48550/arXiv.2507.10518)

Dottorini, D., Calabro, A., Pentericci, L., et al. 2025, *A&A*, 698, A234, doi: [10.1051/0004-6361/202453267](https://doi.org/10.1051/0004-6361/202453267)

Dunlop, J. S., McLure, R. J., Robertson, B. E., et al. 2012, *MNRAS*, 420, 901, doi: [10.1111/j.1365-2966.2011.20102.x](https://doi.org/10.1111/j.1365-2966.2011.20102.x)

Dunlop, J. S., Rogers, A. B., McLure, R. J., et al. 2013, *MNRAS*, 432, 3520, doi: [10.1093/mnras/stt702](https://doi.org/10.1093/mnras/stt702)

Elíasdóttir, Á., Limousin, M., Richard, J., et al. 2007, arXiv e-prints, arXiv:0710.5636, doi: [10.48550/arXiv.0710.5636](https://doi.org/10.48550/arXiv.0710.5636)

Endsley, R., Stark, D. P., Whitler, L., et al. 2023, *MNRAS*, 524, 2312, doi: [10.1093/mnras/stad1919](https://doi.org/10.1093/mnras/stad1919)

—. 2024, *MNRAS*, 533, 1111, doi: [10.1093/mnras/stae1857](https://doi.org/10.1093/mnras/stae1857)

Fan, X., Carilli, C. L., & Keating, B. 2006, *ARA&A*, 44, 415, doi: [10.1146/annurev.astro.44.051905.092514](https://doi.org/10.1146/annurev.astro.44.051905.092514)

Finkelstein, S. L., Papovich, C., Ryan, R. E., et al. 2012a, *ApJ*, 758, 93, doi: [10.1088/0004-637X/758/2/93](https://doi.org/10.1088/0004-637X/758/2/93)

Finkelstein, S. L., Papovich, C., Salmon, B., et al. 2012b, *ApJ*, 756, 164, doi: [10.1088/0004-637X/756/2/164](https://doi.org/10.1088/0004-637X/756/2/164)

Finkelstein, S. L., Ryan, Jr., R. E., Papovich, C., et al. 2015, *ApJ*, 810, 71, doi: [10.1088/0004-637X/810/1/71](https://doi.org/10.1088/0004-637X/810/1/71)

Finkelstein, S. L., D’Aloisio, A., Paardekooper, J.-P., et al. 2019, *ApJ*, 879, 36, doi: [10.3847/1538-4357/ab1ea8](https://doi.org/10.3847/1538-4357/ab1ea8)

Finkelstein, S. L., Bagley, M. B., Ferguson, H. C., et al. 2023, *ApJL*, 946, L13, doi: [10.3847/2041-8213/acad4](https://doi.org/10.3847/2041-8213/acad4)

Flury, S. R., Jaskot, A. E., Ferguson, H. C., et al. 2022a, *ApJ*, 930, 126, doi: [10.3847/1538-4357/ac61e4](https://doi.org/10.3847/1538-4357/ac61e4)

—. 2022b, *ApJ*, 930, 126, doi: [10.3847/1538-4357/ac61e4](https://doi.org/10.3847/1538-4357/ac61e4)

Furtak, L. J., Zitrin, A., Weaver, J. R., et al. 2023, *MNRAS*, 523, 4568, doi: [10.1093/mnras/stad1627](https://doi.org/10.1093/mnras/stad1627)

Gazagnes, S., Chisholm, J., Endsley, R., et al. 2025, *MNRAS*, 540, 2331, doi: [10.1093/mnras/staf768](https://doi.org/10.1093/mnras/staf768)

Gelli, V., Mason, C., & Hayward, C. C. 2024, *ApJ*, 975, 192, doi: [10.3847/1538-4357/ad7b36](https://doi.org/10.3847/1538-4357/ad7b36)

Giallongo, E., Grazian, A., Fiore, F., et al. 2015, *A&A*, 578, A83, doi: [10.1051/0004-6361/201425334](https://doi.org/10.1051/0004-6361/201425334)

Giovinazzo, E., Oesch, P. A., Weibel, A., et al. 2025, <https://arxiv.org/abs/2507.01096>

Gnedin, N. Y. 2000, *ApJ*, 542, 535, doi: [10.1086/317042](https://doi.org/10.1086/317042)

Gnedin, N. Y., Kravtsov, A. V., & Chen, H.-W. 2008, *ApJ*, 672, 765, doi: [10.1086/524007](https://doi.org/10.1086/524007)

Grazian, A., Giallongo, E., Boutsia, K., et al. 2018, *A&A*, 613, A44, doi: [10.1051/0004-6361/201732385](https://doi.org/10.1051/0004-6361/201732385)

—. 2024, *ApJ*, 974, 84, doi: [10.3847/1538-4357/ad6980](https://doi.org/10.3847/1538-4357/ad6980)

Harikane, Y., Ouchi, M., Oguri, M., et al. 2023, *ApJS*, 265, 5, doi: [10.3847/1538-4365/acaaa9](https://doi.org/10.3847/1538-4365/acaaa9)

Henry, A., Berg, D. A., Scarlata, C., Verhamme, A., & Erb, D. 2018, *ApJ*, 855, 96, doi: [10.3847/1538-4357/aab099](https://doi.org/10.3847/1538-4357/aab099)

Inoue, A. K., Shimizu, I., Iwata, I., & Tanaka, M. 2014, *MNRAS*, 442, 1805, doi: [10.1093/mnras/stu936](https://doi.org/10.1093/mnras/stu936)

Izotov, Y. I., Orlitová, I., Schaefer, D., et al. 2016a, *Nature*, 529, 178, doi: [10.1038/nature16456](https://doi.org/10.1038/nature16456)

Izotov, Y. I., Schaefer, D., Thuan, T. X., et al. 2016b, *MNRAS*, 461, 3683, doi: [10.1093/mnras/stw1205](https://doi.org/10.1093/mnras/stw1205)

Izotov, Y. I., Schaefer, D., Worseck, G., et al. 2018a, *MNRAS*, 474, 4514, doi: [10.1093/mnras/stx3115](https://doi.org/10.1093/mnras/stx3115)

Izotov, Y. I., Worseck, G., Schaefer, D., et al. 2018b, *MNRAS*, 478, 4851, doi: [10.1093/mnras/sty1378](https://doi.org/10.1093/mnras/sty1378)

Jaskot, A. E., Silveyra, A. C., Plantinga, A., et al. 2024a, *ApJ*, 972, 92, doi: [10.3847/1538-4357/ad58b9](https://doi.org/10.3847/1538-4357/ad58b9)

—. 2024b, *ApJ*, 973, 111, doi: [10.3847/1538-4357/ad5557](https://doi.org/10.3847/1538-4357/ad5557)

Kassiola, A., & Kovner, I. 1993, *ApJ*, 417, 450, doi: [10.1086/173325](https://doi.org/10.1086/173325)

Katz, H., Cameron, A. J., Saxena, A., et al. 2025a, The Open Journal of Astrophysics, 8, 104, doi: [10.33232/001c.142570](https://doi.org/10.33232/001c.142570)

Katz, H., Rey, M. P., Cadiou, C., et al. 2025b, arXiv e-prints, arXiv:2510.05201, doi: [10.48550/arXiv.2510.05201](https://doi.org/10.48550/arXiv.2510.05201)

Kokorev, V., Atek, H., Chisholm, J., et al. 2025, ApJL, 983, L22, doi: [10.3847/2041-8213/adc458](https://doi.org/10.3847/2041-8213/adc458)

Korber, D., Chemerynska, I., Furtak, L. J., et al. 2025, arXiv e-prints, arXiv:2510.04771, doi: [10.48550/arXiv.2510.04771](https://doi.org/10.48550/arXiv.2510.04771)

Kravtsov, A., & Belokurov, V. 2024, arXiv e-prints, arXiv:2405.04578, doi: [10.48550/arXiv.2405.04578](https://doi.org/10.48550/arXiv.2405.04578)

Madau, P., Giallongo, E., Grazian, A., & Haardt, F. 2024, ApJ, 971, 75, doi: [10.3847/1538-4357/ad5ce8](https://doi.org/10.3847/1538-4357/ad5ce8)

Madau, P., & Haardt, F. 2015, ApJL, 813, L8, doi: [10.1088/2041-8205/813/1/L8](https://doi.org/10.1088/2041-8205/813/1/L8)

Mascia, S., Pentericci, L., Calabro, A., et al. 2023, A&A, 672, A155, doi: [10.1051/0004-6361/202345866](https://doi.org/10.1051/0004-6361/202345866)

—. 2024, A&A, 685, A3, doi: [10.1051/0004-6361/202347884](https://doi.org/10.1051/0004-6361/202347884)

Mason, C. A., Chen, Z., Stark, D. P., et al. 2025, arXiv e-prints, arXiv:2501.11702, doi: [10.48550/arXiv.2501.11702](https://doi.org/10.48550/arXiv.2501.11702)

Mason, C. A., Naidu, R. P., Tacchella, S., & Leja, J. 2019, MNRAS, 489, 2669, doi: [10.1093/mnras/stz2291](https://doi.org/10.1093/mnras/stz2291)

Mason, C. A., Trenti, M., & Treu, T. 2023, MNRAS, 521, 497, doi: [10.1093/mnras/stad035](https://doi.org/10.1093/mnras/stad035)

Matthee, J., Naidu, R. P., Pezzulli, G., et al. 2022, MNRAS, 512, 5960, doi: [10.1093/mnras/stac801](https://doi.org/10.1093/mnras/stac801)

McKinney, J., Cooper, O. R., Casey, C. M., et al. 2025, ApJL, 985, L21, doi: [10.3847/2041-8213/add15d](https://doi.org/10.3847/2041-8213/add15d)

McQuinn, M. 2016, ARA&A, 54, 313, doi: [10.1146/annurev-astro-082214-122355](https://doi.org/10.1146/annurev-astro-082214-122355)

Morales, A., Finkelstein, S., Bagley, M., et al. 2023, in American Astronomical Society Meeting Abstracts, Vol. 241, American Astronomical Society Meeting Abstracts #241, 249.04

Morales, A. M., Finkelstein, S. L., Leung, G. C. K., et al. 2024, ApJL, 964, L24, doi: [10.3847/2041-8213/ad2de4](https://doi.org/10.3847/2041-8213/ad2de4)

Muñoz, J. B., Mirocha, J., Chisholm, J., Furlanetto, S. R., & Mason, C. 2024, MNRAS, 535, L37, doi: [10.1093/mnrasl/slae086](https://doi.org/10.1093/mnrasl/slae086)

Naidu, R. P., Tacchella, S., Mason, C. A., et al. 2020, ApJ, 892, 109, doi: [10.3847/1538-4357/ab7cc9](https://doi.org/10.3847/1538-4357/ab7cc9)

Naidu, R. P., Oesch, P. A., van Dokkum, P., et al. 2022, ApJL, 940, L14, doi: [10.3847/2041-8213/ac9b22](https://doi.org/10.3847/2041-8213/ac9b22)

Nanayakkara, T., Glazebrook, K., Jacobs, C., et al. 2023, ApJL, 947, L26, doi: [10.3847/2041-8213/acfb9](https://doi.org/10.3847/2041-8213/acfb9)

Ouchi, M., Mobasher, B., Shimasaku, K., et al. 2009a, ApJ, 706, 1136, doi: [10.1088/0004-637X/706/2/1136](https://doi.org/10.1088/0004-637X/706/2/1136)

Ouchi, M., Ono, Y., Egami, E., et al. 2009b, ApJ, 696, 1164, doi: [10.1088/0004-637X/696/2/1164](https://doi.org/10.1088/0004-637X/696/2/1164)

Pahl, A. J., Shapley, A., Steidel, C. C., et al. 2023, MNRAS, 521, 3247, doi: [10.1093/mnras/stad774](https://doi.org/10.1093/mnras/stad774)

Papovich, C., Cole, J. W., Hu, W., et al. 2025, arXiv e-prints, arXiv:2505.08870, doi: [10.48550/arXiv.2505.08870](https://doi.org/10.48550/arXiv.2505.08870)

Planck Collaboration, Adam, R., Aghanim, N., et al. 2016, A&A, 596, A108, doi: [10.1051/0004-6361/201628897](https://doi.org/10.1051/0004-6361/201628897)

Prieto-Lyon, G., Strait, V., Mason, C. A., et al. 2023, A&A, 672, A186, doi: [10.1051/0004-6361/202245532](https://doi.org/10.1051/0004-6361/202245532)

Raiter, A., Schaefer, D., & Fosbury, R. A. E. 2010, A&A, 523, A64, doi: [10.1051/0004-6361/201015236](https://doi.org/10.1051/0004-6361/201015236)

Roberts-Borsani, G., Treu, T., Shapley, A., et al. 2024, ApJ, 976, 193, doi: [10.3847/1538-4357/ad85d3](https://doi.org/10.3847/1538-4357/ad85d3)

Robertson, B. E. 2022, ARA&A, 60, 121, doi: [10.1146/annurev-astro-120221-044656](https://doi.org/10.1146/annurev-astro-120221-044656)

Robertson, B. E., Ellis, R. S., Furlanetto, S. R., & Dunlop, J. S. 2015, ApJL, 802, L19, doi: [10.1088/2041-8205/802/2/L19](https://doi.org/10.1088/2041-8205/802/2/L19)

Robertson, B. E., Furlanetto, S. R., Schneider, E., et al. 2013, MNRAS, 429, 2456, doi: [10.1093/mnras/sts515](https://doi.org/10.1093/mnras/sts515)

Rogers, A. B., McLure, R. J., Dunlop, J. S., et al. 2014, MNRAS, 440, 3714, doi: [10.1093/mnras/stu558](https://doi.org/10.1093/mnras/stu558)

Rosdahl, J., Blaizot, J., Katz, H., et al. 2022, MNRAS, 515, 2386, doi: [10.1093/mnras/stac1942](https://doi.org/10.1093/mnras/stac1942)

Saldana-Lopez, A., Schaefer, D., Chisholm, J., et al. 2022, A&A, 663, A59, doi: [10.1051/0004-6361/202141864](https://doi.org/10.1051/0004-6361/202141864)

—. 2023, MNRAS, 522, 6295, doi: [10.1093/mnras/stad1283](https://doi.org/10.1093/mnras/stad1283)

Saldana-Lopez, A., Hayes, M. J., Le Reste, A., et al. 2025, arXiv e-prints, arXiv:2504.07074, doi: [10.48550/arXiv.2504.07074](https://doi.org/10.48550/arXiv.2504.07074)

Saxena, A., Cameron, A. J., Katz, H., et al. 2024, arXiv e-prints, arXiv:2411.14532, doi: [10.48550/arXiv.2411.14532](https://doi.org/10.48550/arXiv.2411.14532)

Schaerer, D., & Pelló, R. 2005, MNRAS, 362, 1054, doi: [10.1111/j.1365-2966.2005.09373.x](https://doi.org/10.1111/j.1365-2966.2005.09373.x)

Shipley, H. V., Lange-Vagle, D., Marchesini, D., et al. 2018, ApJS, 235, 14, doi: [10.3847/1538-4365/aaacce](https://doi.org/10.3847/1538-4365/aaacce)

Simmonds, C., Tacchella, S., Maseda, M., et al. 2023, MNRAS, 523, 5468, doi: [10.1093/mnras/stad1749](https://doi.org/10.1093/mnras/stad1749)

Simmonds, C., Tacchella, S., Hainline, K., et al. 2024, MNRAS, 535, 2998, doi: [10.1093/mnras/stae2537](https://doi.org/10.1093/mnras/stae2537)

Singha, M., Malhotra, S., & Ely Rhoads, J. 2025, arXiv e-prints, arXiv:2510.26990, doi: [10.48550/arXiv.2510.26990](https://doi.org/10.48550/arXiv.2510.26990)

Steidel, C. C., Bogosavljević, M., Shapley, A. E., et al. 2018, ApJ, 869, 123, doi: [10.3847/1538-4357/aaed28](https://doi.org/10.3847/1538-4357/aaed28)

Topping, M. W., Stark, D. P., Endsley, R., et al. 2024, MNRAS, 529, 4087, doi: [10.1093/mnras/stae800](https://doi.org/10.1093/mnras/stae800)

Trebitsch, M., Blaizot, J., Rosdahl, J., Devriendt, J., & Slyz, A. 2017, MNRAS, 470, 224, doi: [10.1093/mnras/stx1060](https://doi.org/10.1093/mnras/stx1060)

Verhamme, A., Orlitová, I., Schaefer, D., & Hayes, M. 2015, A&A, 578, A7, doi: [10.1051/0004-6361/201423978](https://doi.org/10.1051/0004-6361/201423978)

Weaver, J. R., Cutler, S. E., Pan, R., et al. 2024, ApJS, 270, 7, doi: [10.3847/1538-4365/ad07e0](https://doi.org/10.3847/1538-4365/ad07e0)

Zackrisson, E., Inoue, A. K., & Jensen, H. 2013, ApJ, 777, 39, doi: [10.1088/0004-637X/777/1/39](https://doi.org/10.1088/0004-637X/777/1/39)

Zhao, R. J., & Furlanetto, S. R. 2024, JCAP, 2024, 018, doi: [10.1088/1475-7516/2024/09/018](https://doi.org/10.1088/1475-7516/2024/09/018)

Zitrin, A., Fabris, A., Merten, J., et al. 2015, ApJ, 801, 44, doi: [10.1088/0004-637X/801/1/44](https://doi.org/10.1088/0004-637X/801/1/44)